



## Article

# Satellite Magnetism Suggests a Complex Geothermal Heat Flux Pattern beneath the Greenland Ice Sheet

Mick Emil Kolster <sup>1,\*</sup> , Arne Døssing <sup>1</sup> and Shfaqat Abbas Khan <sup>2</sup>

<sup>1</sup> DTU Space, Division of Geomagnetism and Geospace, CMAGTRES Group, The Technical University of Denmark, 2800 Kongens Lyngby, Denmark

<sup>2</sup> DTU Space, Division of Geodesy and Earth Observation, The Technical University of Denmark, 2800 Kongens Lyngby, Denmark

\* Correspondence: memkol@space.dtu.dk

**Abstract:** Geothermal heat flow is key to unraveling several large-scale geophysical systems, including the inner workings of the Greenlandic ice sheet, and by extension, the possibility of understanding the past and prior global climate. Similarly, it could provide insight into the paleo-trace of the Icelandic mantle plume, which in turn is integral in answering long-standing questions on the origin of mountains in western and eastern Greenland and in Norway. This study documents the results from an intra-scientific field approach, which combines geological, petrophysical, and satellite magnetic field data in a nonlinear probabilistic inversion. These results include Curie depths with associated uncertainties and Geothermal Heat Flux estimates. While baselines remain challenging to evaluate due to the strong nonlinearity of the problem posed, stress testing reveals a high robustness of the predicted spatial variations, which largely disagree with the classic straightforward northwest–southeast or east–west plume trace across Greenland. Instead, our results indicate a complex heat flux pattern, including a localized region with anomalously heightened heat flux near the origin of the Northeast Greenland Ice Stream.

**Keywords:** probabilistic inversion; icelandic plume trace; geothermal heat flux; Greenland; satellite magnetic data; Northeast Greenland Ice Stream; NEGIS; SIPPI



**Citation:** Kolster, M.E.; Døssing, A.; Khan, S.A. Satellite Magnetism

Suggests a Complex Geothermal Heat Flux Pattern beneath the Greenland Ice Sheet. *Remote Sens.* **2023**, *15*, 1379. <https://doi.org/10.3390/rs15051379>

Academic Editor: Fridon Shubitidze

Received: 20 December 2022

Revised: 20 February 2023

Accepted: 21 February 2023

Published: 28 February 2023



**Copyright:** © 2023 by the authors. Licensee MDPI, Basel, Switzerland. This article is an open access article distributed under the terms and conditions of the Creative Commons Attribution (CC BY) license (<https://creativecommons.org/licenses/by/4.0/>).

## 1. Introduction

Seismic tomography models are indicative of an upper [1] or whole-mantle [2,3] low-velocity zone beneath Iceland. This inferred mantle plume has been linked to the sub-aerial emergence of Iceland in the Northeast Atlantic during the Neogene [1,2] as well as the formation of high coastal mountains and widespread breakup-related flood basalts along the passive margins surrounding the North Atlantic (Figure 1) [4–10].

The Iceland plume is generally thought to have thinned and heated the interior of the Greenland lithosphere due to a predicted northwest-directed plate movement of Greenland [11] prior to the break-up of the North Atlantic [10–14]. However, the interaction of the plume with the interior of Greenland remains a topic of debate. A recent study [10] argues against the classical idea of a plume track across Greenland and suggests that the widespread, seemingly contemporaneous, volcanism in western and eastern Greenland around 60 Ma can be explained by a direct interaction of a mantle plume with seafloor spreading ridges, regional mantle flow, and an already thinned lithosphere along an east–west corridor across central Greenland. Nonetheless, determining areas of interior Greenland that may have had direct interaction with the Iceland plume is critical to model the impact of a potential plume-related heat anomaly on the past and future evolution of the Greenland Ice Sheet. Numerical ice-sheet models need input data, including environmental variables such as Geothermal Heat Flux (GTHF). The importance of a plume-related heat anomaly is exemplified in [15], who suggests that the Northeast Greenland ice stream is likely initiated by a geothermal heat flux anomaly close to the ice divide, left behind by the

movement of Greenland over the Icelandic plume. In general, the Northeast Greenland ice stream is not accurately represented in ice-sheet models. In particular, it is challenging for ice flow models to capture high velocities far inland at the onset of the ice stream. The Northeast Greenland ice stream is characterized by an exceptional fast-flowing main trunk that is more than 600 km long and about 30–50 km wide [16].

Several different methods have so far been applied in the attempt to determine the Icelandic mantle plume trace, including estimates of Curie depths and GTHF models from satellite magnetic data [17] or from compilations of air- and ship-borne magnetic data [18]. Such estimation efforts are typically challenging to perform, and must often deal with unavoidable sources of uncertainty which can hamper the estimation process. These are primarily due to circumstances which either cannot, or are vastly impractical, to measure in situ (e.g., requirements of information from beneath ice sheets, or information on crustal parameters which would require measurements deep within the crust). The primary impracticality is often the density of information required in order to account for spatial variations in physical parameters required as input in the modeling process, e.g., magnetic properties and susceptibility of the crust throughout. Left with no easy options, researchers must often navigate a host of challenges in order to generate useful models. Such challenges thus often include, e.g., high uncertainties in underlying physical parameters on which a model depends, or availability of only coarse information and/or parameter estimates, all of which can lead to a degradation in the accuracy of the resultant models. Furthermore, model validation is typically equally challenging to perform for many of the same reasons, and researchers are often left with little to no reliable options for validation, e.g., again due to the impracticality of gathering sufficiently dense data of geothermal heat flow measurements. As such, the model uncertainty is often left largely unvalidated or even unassessed, since such efforts are simply not feasible given the data and methods available. Examples of inhibiting factors may include the lack of uncertainty estimates on modeling inputs, the impracticality of accurately evaluating the impact of employed assumptions into the modeling output, or that the circumstances of the physical property to be modeled inhibits extraction of meaningful uncertainty estimates (e.g., due to the requirement of regularization when faced with under-determined systems). As such, while researchers often make an effort to estimate uncertainties, only parts of the aggregate uncertainty may be possible to evaluate (e.g., as in [18], where an effort is made to estimate uncertainties). Regardless, the uncertainty estimates are typically ambiguous, due to a lack of suitable external validation points. A prime example of this occurs in heat flux modeling, where validation [17] or even tuning [19] is sometimes attempted against point-measurements of heat flux, such as those obtained from ice boreholes, which are only available in scarce quantities in the interior of Greenland [20]. This form of validation is generally carried out for lack of a better alternative, but the scarcity of the data unfortunately means that the measured heat flux cannot necessarily be considered representative outside their immediate vicinity (which may be very local, given the possibility of anomalous heat flux at the given measurement location). Ref. [21] assessed a number of existing Geothermal Heat Flux models by modeling their ability to reconstruct current Greenlandic Ice Sheet thicknesses. Although the direct link between GTHF model and validation data is less clear due to the interim modeling, the process enables validation on more suitable data, such as spatially well-distributed observations of Greenlandic Ice Sheet thicknesses (e.g., [22]). The authors of [21] highlighted the variability across some existing GTHF models, and found that a uniform heat flux across Greenland outperformed any of the evaluated models. We find that the uncertainties associated with Geothermal Heat flux raise serious questions regarding their use to predict, e.g., plume traces, and seek to challenge the current modeling meta through an interdisciplinary, uncertainty-based modeling method.

Our multi-disciplinary approach incorporates *a priori* geophysical, petrophysical, and geological information, with satellite magnetics comprising the main dataset. We include uncertainty evaluations, including data uncertainties, and as few assumptions as possible.

The main modeling consists of a probabilistic inversion [23], for which we utilize the extended Metropolis algorithm of [24], as implemented in the SIPPI toolbox of [25,26].

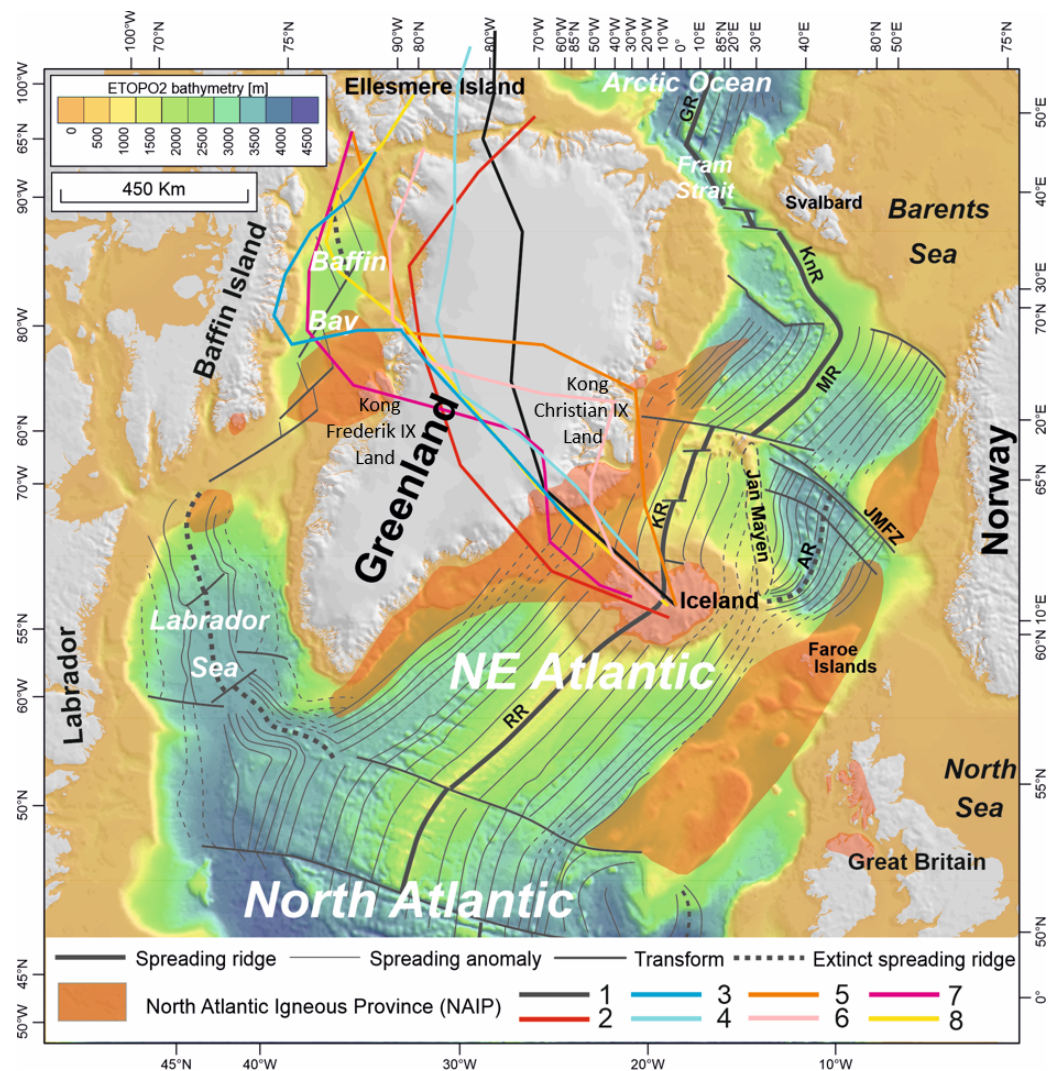


**Figure 1.** Tectonic and geological overview of the North Atlantic–Labrador Sea/Baffin Bay area (modified from [6]). Colored lines (numbered 1–8) across Greenland show examples of suggested traces of the Iceland plume since Early Cretaceous: 1: [12,18]. 2: [27]—fixed. 3: [13]. 4: [28]. 5: [29]—moving. 6: [30]—moving. 7: [30]—fixed. 8: [31]. Highlighted polygons: extent of North Atlantic Igneous Province (NAIP). Abbreviations: AR, Aegir Ridge; GR, Gakkel Ridge; JMFZ, Jan Mayen Fracture Zone; KnR, Knipovich Ridge; KR, Kolbeinsey Ridge; MR, Mohns Ridge; RR, Reykjanes Ridge.

## 2. Method

The nonlinear forward problem is typically generalized as a system of equations  $\mathbf{d} = g(\mathbf{m}) + \varepsilon$ , where  $\mathbf{m}$  is a vector of unknown model parameters,  $\mathbf{d}$  contains (known) data, and  $g()$  is the nonlinear function which predicts  $\mathbf{d}$  given  $\mathbf{m}$ , to some error  $\varepsilon$ .

We seek to infer magnetic crustal thicknesses from the geomagnetic crustal field, as defined by the LCS-1 model of [32]. Our problem parameterization largely follows [33]; it is obtained by subdividing the (assumed spherical) Earth's surface into 25,002 roughly equal-area hexagonal columns (a Goldberg tessellation, via icosahedral subdivision of frequency 50), and using the Equivalent Source Magnetic Dipole method of [34] to describe the magnetic response of each column, using a dipole placed at the center of each column surface. Our unknown model parameters are thus the individual magnetic crustal thick-

nesses  $\tau$  and individual magnetic susceptibilities  $\chi$  of each column. The resultant forward problem is expressed by Equation (1):

$$\underbrace{\begin{bmatrix} \mathbf{B}_{q_1} \\ \mathbf{B}_{q_2} \\ \vdots \\ \mathbf{B}_{q_N} \end{bmatrix}}_{\text{Data vector } \boldsymbol{\beta}} = \underbrace{\begin{bmatrix} \boldsymbol{\Gamma}_{d_1 \rightarrow q_1} & \boldsymbol{\Gamma}_{d_2 \rightarrow q_1} & \cdots & \boldsymbol{\Gamma}_{d_N \rightarrow q_1} \\ \boldsymbol{\Gamma}_{d_1 \rightarrow q_2} & \boldsymbol{\Gamma}_{d_2 \rightarrow q_2} & \cdots & \boldsymbol{\Gamma}_{d_N \rightarrow q_2} \\ \vdots & \vdots & \ddots & \vdots \\ \boldsymbol{\Gamma}_{d_1 \rightarrow q_N} & \boldsymbol{\Gamma}_{d_2 \rightarrow q_N} & \cdots & \boldsymbol{\Gamma}_{d_N \rightarrow q_N} \end{bmatrix}}_{\text{Computation and filtering kernel } \boldsymbol{\Lambda}} \underbrace{\begin{bmatrix} \chi_{d_1} \tau_{d_1} \\ \chi_{d_2} \tau_{d_2} \\ \vdots \\ \chi_{d_N} \tau_{d_N} \end{bmatrix}}_{\text{Nonlinear function } \delta} + \underbrace{\begin{bmatrix} \varepsilon_1 \\ \varepsilon_2 \\ \vdots \\ \varepsilon_N \end{bmatrix}}_{\text{Error } \boldsymbol{\zeta}} \quad (1)$$

where  $\mathbf{B}_{q_N}$  is a column vector containing magnetic field components at the  $N$ -th query point,  $\chi_{d_N}$  and  $\tau_{d_N}$  are the magnetic susceptibility and magnetic crustal thickness (MCT), respectively, of the crustal column represented by the  $N$ -th dipole, and  $\boldsymbol{\Gamma}_{d_N \rightarrow q_N}$  is a column vector describing the linear relation between the product  $\chi_{d_N} \tau_{d_N}$  and  $\mathbf{B}_{q_N}$ . Solutions to Equation (1) can be approximated through assumptions on the values of  $\chi$  [33], or by collapsing the parameters into the columnar Vertically Integrated Susceptibility  $VIS_{d_n} = \chi_n \tau_n$ , but direct inference of  $\chi_{d_n}$  and  $\tau_{d_n}$  for each of the  $N$  individual columns is clearly non-unique. Based on known geological correlations and dependencies [35–38], we seek to alleviate the non-uniqueness by grouping columns into regions of expected similar crustal composition and, by extension, assumed similar magnetic susceptibilities. Under these assumptions, the forward problem takes the simplified form of Equation (2):

$$\boldsymbol{\beta} = \boldsymbol{\Lambda}(\boldsymbol{\chi}_m \circ \boldsymbol{\tau}) + \boldsymbol{\zeta} \quad (2)$$

where the elements of  $\boldsymbol{\chi} = [\chi_1, \chi_2, \dots, \chi_M]^T$  contains Regional Susceptibilities (RS; identical magnetic susceptibilities for all crustal columns in each of  $M$  crustal regions),  $\boldsymbol{\tau}$  is the vector of individual MCTs, and  $\circ$  denotes the Hadamard product. The assumption of regionally constant magnetic susceptibilities partially alleviates the strong nonlinearity of the problem, but it remains non-unique, leaving Equation (2) essentially unsolvable for practical purposes in the current formulation.

Fortunately, several pieces of relevant a priori information are available for the components of Equation (2). We therefore turn to the probabilistic inversion approach [23,39], and utilize available a priori information as modeling constraints. Probabilistic inversion essentially treats all input and output information as probability density functions. Assuming an independence between data probability densities and model parameter probability densities, the general probabilistic problem relation is Equation (3) [23]:

$$\sigma_M(\mathbf{m}) = k\rho_M(\mathbf{m})L(\mathbf{m}) \quad (3)$$

where  $\sigma_M(\mathbf{m})$  and  $\rho_M(\mathbf{m})$  are the posterior and prior probability distributions of the model parameters, respectively,  $L(\mathbf{m})$  is the likelihood function, and  $k$  is a normalizing constant. We solve Equation (3) through the extended Metropolis algorithm of [24], which enables sampling of  $\sigma_M(\mathbf{m})$  if three conditions are met:

1. Samples can be drawn from the prior distribution;
2. The forward problem can be posed in such a way that it is solvable;
3. The likelihood of each solution can be evaluated, i.e., through evaluation of the data residual against a noise model.

A solvable forward problem was defined by Equation (2), leaving the prior distribution and likelihood evaluation criteria. Regarding the prior distribution, we first seek to reduce the regions in which a priori information is required. This is accomplished by subdividing the inversion into two parts: a nonlinear portion comprises Greenland and its vicinity, where we solve Equation (3), and a linear portion, which comprises the remainder of the Earth’s crust, solved using the LSQR algorithm of [40]. Expressing the crustal field in a

spherical harmonic expansion, we can view this as a partitioning of contributions to the Gauss coefficients, as shown in Equation (4):

$$\begin{bmatrix} g_n^m \\ h_n^m \end{bmatrix} \approx \frac{1}{R_\oplus} \left( \frac{R_i}{R_\oplus} \right)^{n+1} \frac{2n+1}{4\pi} \sum_{i=1}^{N_i} (V_{lin}(\mathbf{r}_i) + V_{non}(\mathbf{r}_i)) \begin{bmatrix} \cos(m\varphi_i) \\ \sin(m\varphi_i) \end{bmatrix} P_n^m(\cos(\vartheta_i)) dS_i \quad (4)$$

where  $V_{lin}(\mathbf{r}_i)$  and  $V_{non}(\mathbf{r}_i)$  are the contributions to the magnetic potential at all query points  $\mathbf{r}_i$  from dipoles in the linear and nonlinear regions, respectively. Additional details on the subdivision are provided Appendix A.

We construct prior probability densities of the magnetic crustal thickness from tomography-inferred Moho depths [41] and the CRUST1.0 model [42], while crustal magnetic susceptibility priors are drawn from prior studies, which include the scarce petro-physical measurements available in Greenland and geologically related regions in Finland, Canada and Norway, and oceanic susceptibility estimates [43–61]. The compilation of prior information is structured so that the MCT of each crustal column, and the RS for each region, is encoded as individual 1D Gaussian prior probability distributions. An overview of the complete problem parameterization is provided in Appendix A, while further information on construction of prior distributions and their parameters is provided in Appendix B.

The data for the inversion are sampled from the satellite data-derived LCS-1 crustal magnetic field model [32], which we first reduce by subtracting the RVIM0 oceanic remanence model of [62]. Due to the associated computational requirements, data for all runs are obtained by evaluating the LCS-1 model at 300 km altitude for spherical harmonic degrees  $16 \leq n \leq 80$ . Coupled with the chosen crustal parameterization, we thereby assume that the ensemble of dipoles, each representing a hexagonal crustal columns approximately  $\sim 160$  km wide at the surface, can accurately represent the magnetic crust to within specified uncertainties when viewed from satellite altitude. In order to comply with the input data, modeling results are solely evaluated for the same spherical harmonic range as the data (all contributions to the total model response outside of this range are disregarded). The altitude of evaluation was selected to approximately match the altitude of the original data collection. Given this altitude, evaluation of the LCS-1 model past degree 80 provides progressively lower contributions to the measured magnetic field, due to the rapidly declining power at higher spherical harmonic degrees. On average, the difference between evaluating the LCS-1 model at 300 km altitude up until spherical harmonic degree 80 and spherical harmonic degree 160 is 0.25 nT for the radial component, 0.17 nT for the co-latitudinal component, and 0.17 nT for the longitudinal component.

We assume a purely induced crustal magnetization, with the inducing (core) field taken as spherical harmonic degrees  $1 \leq n \leq 15$  of the CHAOS-6 model of [63]. Likelihood evaluation is enabled by associating each datapoint drawn from the LCS-1 model of [32] with identical standard deviations, i.e., we treat each datapoint as a 1D Gaussian. Since direct evaluation of the data error is not straightforward, several data standard deviation values were tested across multiple different inversions.

Due to the uncertainties concerning crustal thermal parameters required to convert MCT to GTHF, we find complex GTHF modeling unwarranted. Geothermal heat flux estimates from a single-layer 1D (vertical) heat flow model, with a crustal heat production model adopted from [64], and thermal parameters adopted from [65], are provided to ease interpretation, but due to the complexity and thus large uncertainty associated with such modeling (e.g., [66–69]), the underlying MCT maps are considered the primary result of this study.

A graphical overview of the data preparation, parameterization, and processing pipeline utilized in the study is provided by Figure 2. Further details, including the full equations employed in this study, are provided in Appendices A–D.

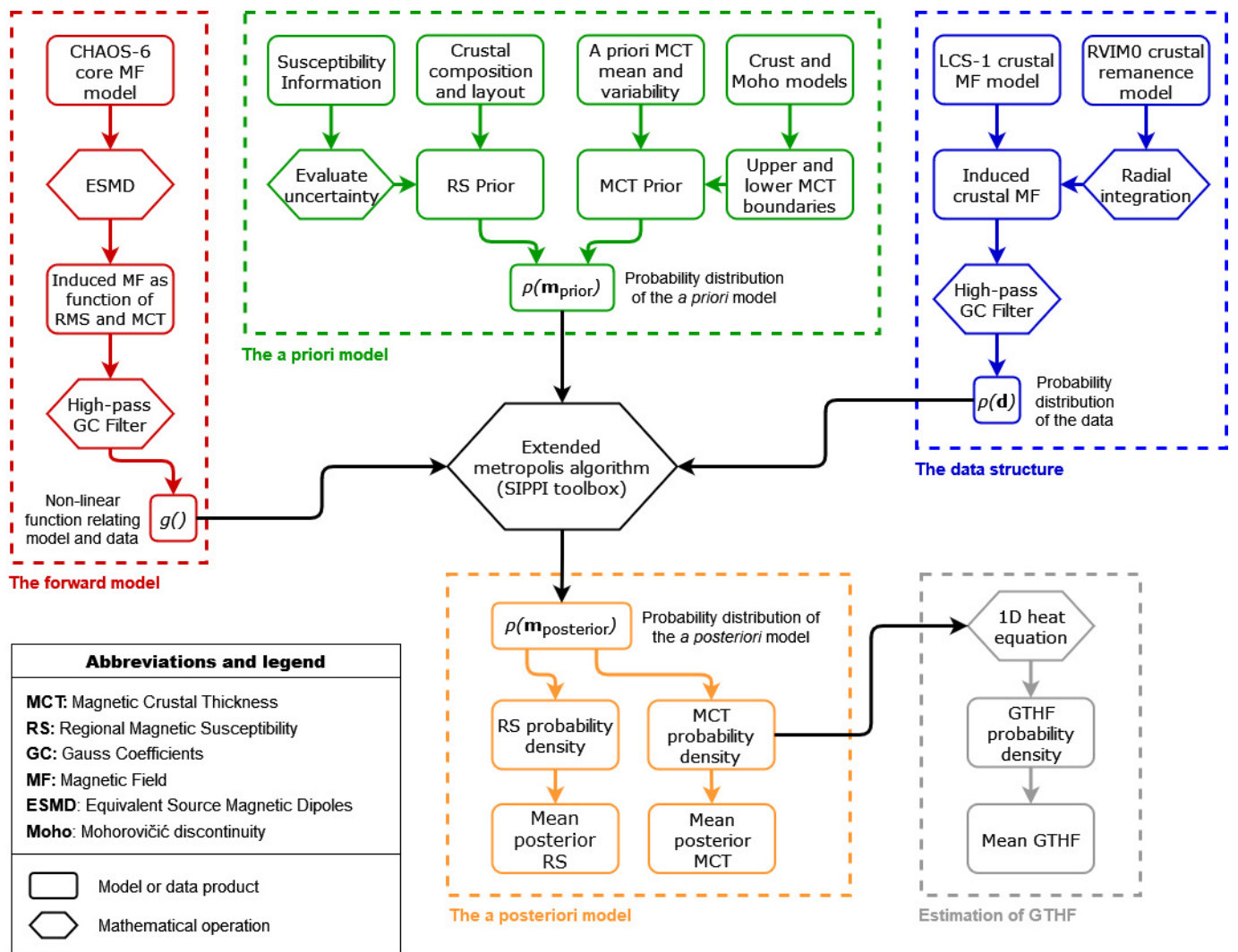
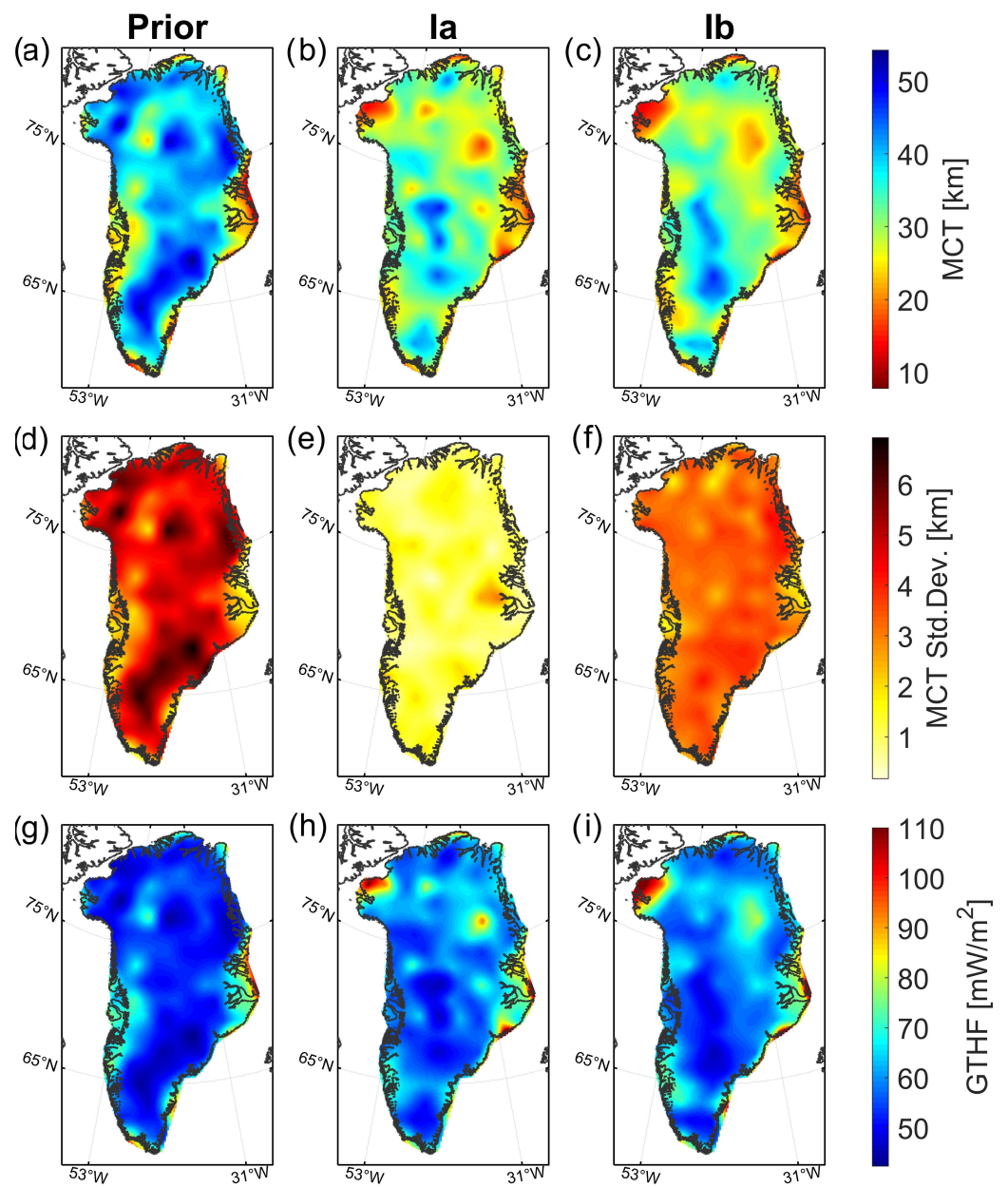


Figure 2. Overview of the processing pipeline employed in this study.

### 3. Results

Ten different modeling runs, with differing prior distributions and sampling strategies, were performed. Of these, two were primary runs (denoted Ia and Ib), while the remaining eight (denoted II through IX) were robustness checks with progressively perturbed initial conditions, performed to assess potential impacts of any uncertainties in the governing parameters obtained of the prior and data distributions. Concerns over strong correlations across posterior samples in run Ia led to run Ib being conducted using relaxed conditions, to the point that a few MCT parameters even re-sampled the prior. Run Ib exhibited a high degree of exploration, while retaining overall similarities with run Ia, suggesting that both provide relevant realizations of the posterior model. Overall, we consider run Ib to be the best model based on the amount of posterior samples drawn and its more relaxed conditions. Figure 3 shows the prior MCT and its equivalent GTHF alongside results from the primary runs, while results from the robustness checks are shown in Figure 4. An overview of the data fit of the posterior model from Ib is shown in Figure 5. Additional information, including the specific parameters for each run, is provided in Appendix C.



**Figure 3.** Overview of main MCT results from the probabilistic solver. The results have been interpolated and clipped to continental Greenland. Subfigures (a–c) present the mean Magnetic Crustal Thickness from the prior model, posterior model Ia, and posterior model Ib, respectively. Subfigures (d–f) show the respective uncertainty estimates (standard deviations) for (a–c). Subfigures (g–i) show estimated Geothermal Heat Flux associated with each posterior mean. The range of the colorbar in the lower row is exceeded sporadically, primarily at the continental limit in northwestern Greenland. Further details are provided in Appendix D.

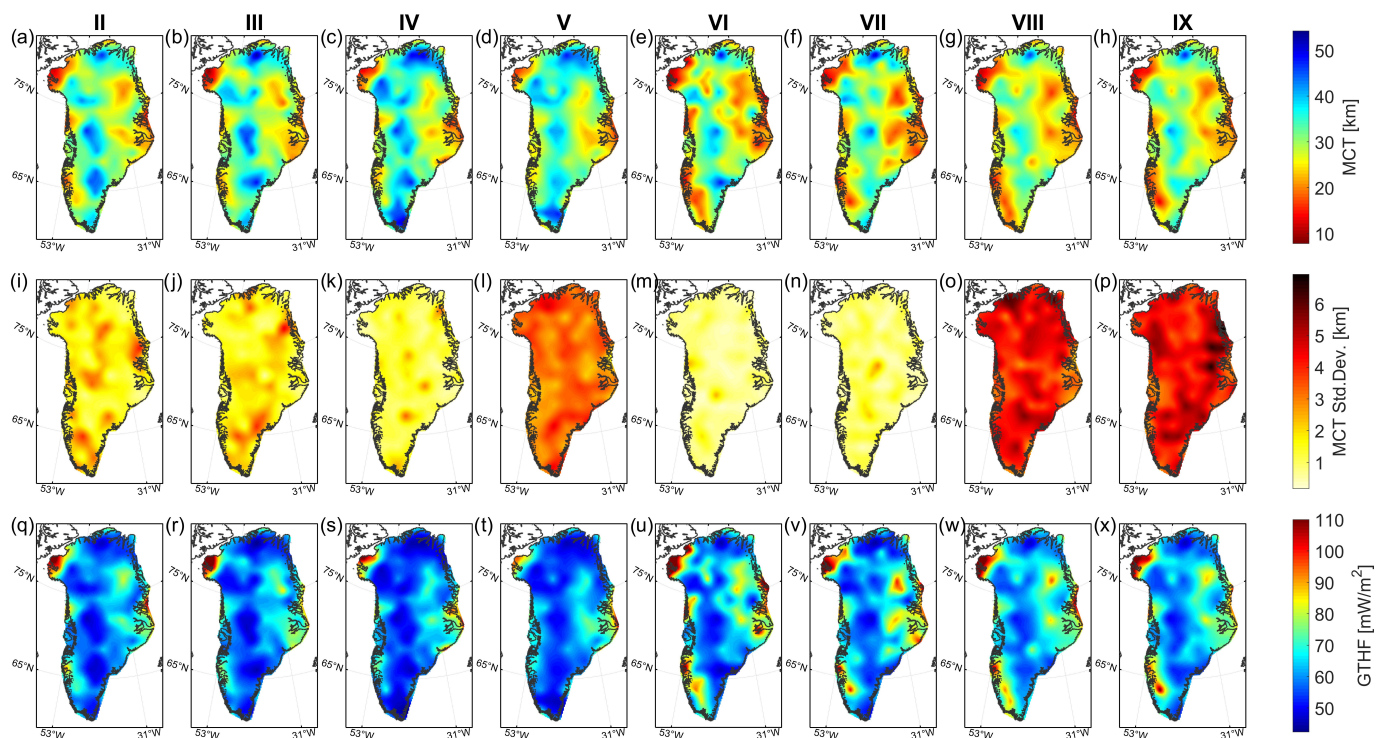


**Figure 4.** Overview of posterior mean realizations from the probabilistic solver. The results have been interpolated and clipped to continental Greenland to ease visual interpretation. Subfigures (a–h) present the mean posterior Magnetic Crustal Thickness. Subfigures (i–p) show the corresponding posterior uncertainty estimates predicted by the solver, providing insight into how prior and data uncertainties propagate into the posterior model. Subfigures (q–x) contain estimated Geothermal Heat Flux associated with each posterior mean. Colorbar ranges are the same as in Figure 3. The range of the colorbar in the lower row is exceeded sporadically, primarily at the continental limit in northwestern Greenland. Columns are ordered according to the degree of perturbation, i.e., column IX corresponds to the largest deviation from original initial conditions. Further details are provided in Appendix D.

The apparent low MCT standard deviation from run Ia may suggest that an overly constrained sampling has been enforced, given the relatively large amount of model parameters used to fit spherical harmonic degree  $16 \leq n \leq 80$  data. As such, Run Ia may exhibit some degree of over-fitting, which could also explain the initial suspicions of insufficient model space exploration. Note the difference when using a more exploratory sampling in run Ib, despite using the same initial conditions as run Ia. The similarities between Figures 3 and 4, especially the strong correlation of features across their upper and lower rows, reveal a strong robustness in the predicted MCT structures, and by extension, the derived GTHF estimates. Feature robustness is seen across both strictly and loosely constrained models (which exhibit low and high predicted MCT standard deviations, respectively), and regardless of the initial condition perturbations evaluated, suggesting that the nonlinearity of Equation (1) has been reduced to a point where conclusions may be drawn. Although this does not allow hard conclusions on absolute MCT or GTHF, it provides a general estimate of the former, upon which general conclusions regarding patterns in both MCT and GTHF can be made, given their inverse correlation.

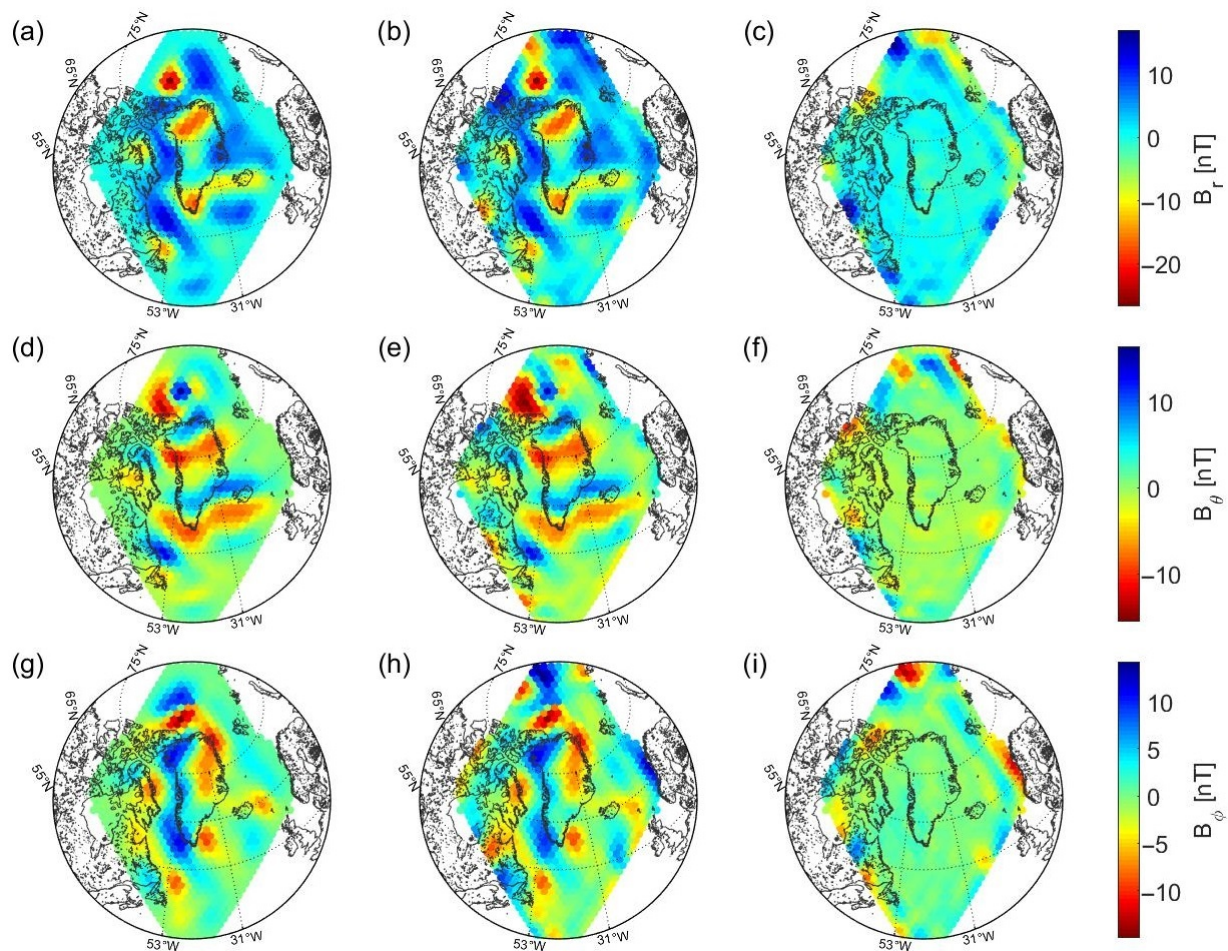


**Figure 5.** Data and model fit for model Ib. Subfigures (a,b) depict the radial component of the LCS-1 model (the data) and modeling run Ib, respectively, while subfigure (c) depicts the data residual obtained by subtracting (b) from (a). Subfigures (d,e) depict the co-latitude component of the LCS-1 model (the data) and modeling run Ib, respectively, while subfigure (f) depicts the data residual obtained by subtracting (e) from (d). Subfigures (g,h) depict the longitudinal component of the LCS-1 model (the data) and modeling run Ib, respectively, while subfigure (i) depicts the data residual obtained by subtracting (h) from (g). The heightened data misfit visible along the edges stems from the overlap with the linear region (see Appendix A for further details). All data, model responses, and residuals are evaluated at an altitude of 300 km, i.e., at the same altitude used in the inversion process.

#### 4. Discussion

The nonlinear dependency between MCT and the RS for each region hampers explicit determination of their absolute values, and by extension, absolute GTHF estimation (which is also severely hampered by a lack of knowledge on the thermal properties and layout of the crust). As such, we do not consider it reasonable to estimate the absolute values of MCT, RS, and GTHF based on this study alone. However, relative variations in the robust MCT features provide unique information, and through the inverse correlation between MCT and GTHF, relative traits should be transferable across the two, e.g., as seen across the MCT and GTHF estimates in Figures 3 and 4. Except for the structures along the west coast of the southern tip of Greenland, the relative MCT features across all model runs are generally in alignment; we consider this to be our most consequential result.

The parameterization and input data were selected with regard to both computational and investigative feasibility. The latter depends on the assumption that the crustal structures of interest, e.g., mantle plume traces, can be resolved using the magnetic field information

utilized, and that corresponding surface features can be captured using  $\sim 160$  km wide surface tiles. While the plume stem is believed to be narrow, perhaps 100 km across, and extending down to at least 400–650 km beneath the surface, the plume head may exceed 1000 km in width [70,71]. We therefore consider the parameterization to be reasonable for the performed investigation. By fixing the dipole representing each column to the surface, we potentially incur a slight bias in the result. Should this be the case, the bias effect will depend on the MCT; large MCT values in the results may be slight over-estimates, while effects on areas with shallow MCT estimates will be limited. However, considering that the estimated Curie isotherms all relatively shallow when compared to the altitude of the data, we expect that any such potential bias effects will be, at least partially, encompassed by the specified uncertainties.

Note that while there is a clash between essentially-equal-area tessellations and spherical harmonic expansions when nearing the poles (since resolved wavelengths along parallels decrease), any resultant effects only concern variations in one direction, are confined to small wavelengths or areas near the poles, and are expected to be encompassed by the specified data uncertainties to begin with. We therefore expect the influence of such effects to be minor or even negligible, as supported by the high robustness of features towards the poles. The data are thus considered suitable for the parameterization and performed investigations.

Although we argue for the robustness features shown across the MCT maps are indeed real, there are still a few underlying assumptions that could have biased the results. Of these, the subdivision used for susceptibility regions is the hardest constraint, and could carry a significant weight. Especially the large C. Greenland region could prove to have a significant impact on the results. Regardless, the choice was made to proceed with the employed subdivision, primarily for lack of a better alternative.

#### 4.1. No Clear Trace of a Mantle Plume

Given the assumption that a low MCT reflects thinned lithosphere [72], our model agrees with the general consensus that the Iceland plume withdrew from beneath the Greenland craton in southeastern Greenland, just slightly northeast of the Kangerlussuaq fiord. However, it does not support a straightforward Iceland plume track across the interior of Greenland [11,12,18], such as a simple northwest–southeast or west–east mantle plume trace. Stress testing of the models revealed these findings to be robust across parameter estimates, see Figure 4.

Comparison with the results of [17] reveal similarities in the two satellite data-based models. The most prominent similarities are the low MCT in both Kong Christian IX land and Kong Frederik IX land (locations shown in Figure 1), the ridge of high MCT stretching north–south through north and central western Greenland, the heightened MCT along the southeastern shoreline, and to some extent, the high MCT in northeastern Greenland.

A particularly impactful realization from our results concerns the current modeling meta of plume trace anomalies; given only slight regularization or bias, a significant number of potential plume tracks become viable. Any of these could be favored by a given modeling approach, depending on the employed constraints, regularization and/or alternate biasing, and other underlying assumptions. This suggest a rather clear path forward for more reliable Iceland plume track modeling; assumptions, constraints, or regularization should only be applied with extreme prejudice, due to the ease in which their effects could skew or even dominate the results.

#### 4.2. A Robust Heat Flux Anomaly Near NEGIS Origin

All models predict heightened geothermal heat flux beneath the Northeast Greenland Ice Stream (NEGIS), with a significant positive peak immediately beneath its origin. This supports the hypothesis that at least part of NEGIS is driven by an enlarged GTHF. The NEGIS heat flux feature is robust across all modeling runs and consistent with, e.g., [73], who suggested that the melt anomaly beneath NEGIS may be explained by Iceland plume

history. The high melt is further evidenced in radar soundings measurements by [74], who showed a significant anomaly about 700 km upstream glacier at the origin of NEGIS. In general, heat flux beneath Greenland, and in particular, beneath NEGIS is important to map, as it has huge implications for future behavior of the Greenland Ice Sheet and the ice flow dynamics of NEGIS. Greater geothermal heat flux at the base of an ice mass will impact upon its internal thermal regime and the presence of basal melt water.

The heat flux anomaly beneath east Greenland is, likewise, critical for future behavior of the Greenland Ice Sheet and the earth–ice interaction. Geothermal heat flux at the glacier bedrock is evidence of a warm upper mantle, which affects the response of the solid Earth to the deglaciation process, the glacial isostatic adjustment. A warm upper mantle, as in east Greenland, has a low viscosity, which in turn causes the solid Earth to rebound much faster to deglaciation. Instead of over millennia, the solid Earth can rebound tens of meters within a decade. This Earth feedback mechanism has a stabilizing effect on the evolution of marine-terminating glaciers, and highly influences future estimates of sea level rise. The observed positive heat flux anomaly in east Greenland coincides with a low P-wave velocity perturbation while the confined heat flux anomaly beneath does not appear to be resolved in seismic tomography data [75].

In the future, a combined effort with ice-sheet modeling may enable explicit determination of GTHF through optimization of only a small number of constants given relative MCT, e.g., as an extension to GTHF model testing, such as those performed by [21]. We suspect that such a holistic approach may be warranted for, e.g., estimation of general thermal parameters of the crust. In this regard, magnetic data alone may not be sufficient, at least when employed in the form used in this study. The inclusion of additional data types, as well as higher density and better quality magnetic data, may significantly improve MCT and GTHF estimation in the future. Examples of potential sources of data improvement include improved crustal field estimates from satellite magnetic data, and dense high-altitude aeromagnetic data.

Our model is intentionally not constrained using the scarce heat flux measurements available within central Greenland [20], due to the disproportional spatial representation and weight each datapoint would carry in such a scenario. Should even a single GTHF point-measurement stem from a position or area constituting any kind of heat flux outlier, that datapoint could, in turn, skew the model significantly in an area disproportionately larger than the typical length scale of surface GTHF variation.

## 5. Conclusions

Our modeling results consistently predict the existence of a heightened heat flux near the onset of the Northeast Greenland Ice Stream. This may be important for subglacial hydrology and modeling ice dynamics of the northeast Greenland outlet glaciers.

Other robustly predicted features include low MCT (and by correlation high GTHF) along an approximately N–S axis in central eastern to central northern Greenland, peaking around the Northeast Greenland Ice Stream, and scattered regions of low heat flux along a similar axis in western Greenland. Other robust features predicted include a number of areas, including on the north and central coast of western Greenland, with low MCT (and high GTHF), which may be related to a potential plume trace. However, we find no clear evidence for an actual plume trace through Greenland; neither a SE–NW or E–W trending trace, nor any other plume trace.

The results highlight the complexity of the solution space, and suggest that even small biases, e.g., due to regularization or simplifying assumptions, could lead to the unintentional favoring of one potential plume track over others during modeling. The multidisciplinary approach demonstrated in this study provides a novel foundation which may, in time, aid in determining a robust, explicit solution to the geothermal heat flux estimation problem.

**Author Contributions:** Conceptualization, resources, data curation, validation, supervision, project administration, funding acquisition, and writing—review and editing: M.E.K., A.D. and S.A.K. Visualization: M.E.K. and A.D. Software, methodology, formal analysis, investigation, and writing—original draft preparation: M.E.K. All authors have read and agreed to the published version of the manuscript.

**Funding:** This research received no external funding.

**Data Availability Statement:** Model outputs will be hosted openly at <https://ftp.space.dtu.dk/pub/abbas/RemoteSensing2023/> (accessed on 6 December 2021) from the time of publication. The LCS-1 crustal field model of [32] is available for download from <http://www.spacecenter.dk/files/magnetic-models/LCS-1/> (accessed on 6 December 2021). The CHAOS-6 model of [63] is similarly hosted at <http://www.spacecenter.dk/files/magnetic-models/CHAOS-6/> (accessed on 6 December 2021). The RVIM0 oceanic remanence model of [62] was provided by S.M. Masterton upon request. The SIPPI framework of [25,26] is made openly available by T.M. Hansen at <https://github.com/cultpenguin/sippi> (accessed on 6 December 2021).

**Acknowledgments:** The authors thank Professor Thomas Meyer Hansen for providing constructive feedback on the draft manuscript. Professors Christopher C. Finlay and Nils Olsen are thanked for the useful discussions which helped form this study. All modeling runs were performed on the High Performance Computing Cluster at the Technical University of Denmark.

**Conflicts of Interest:** The authors declare no conflict of interest. The funders had no role in the design of the study; in the collection, analyses, or interpretation of data; in the writing of the manuscript, or in the decision to publish the results.

## Abbreviations

The following abbreviations are used in this manuscript:

GTHF	Geothermal Heat Flux
MCT	Magnetic Crustal Thickness
RS	Regional Susceptibility
NEGIS	Northeast Greenland Ice Stream

## Appendix A. Problem Parameterization

The Earth's surface was tessellated using 25,002 roughly equal-area, predominately hexagonal tiles, obtained as the vertices of a recursive icosahedral subdivision with frequency 50 (also known as a Goldberg tessellation, with the necessary pentagons deliberately distanced from Greenland). Each tile spans an area approximately  $\sim 160$  km across, and is considered to be the face of a magnetic crustal column of unknown height (the magnetic Crustal Thickness, or MCT). The magnetic response of each column is parameterized through the Equivalent Source Magnetic Dipole method of [34], where we have kept the dipole positions static at the surface to retain a feasible computational time. The resultant governing equations of the parameterization are largely equivalent to those employed by [33], and depend on the inducing field, magnetic susceptibility, and Magnetic Crustal Thickness, with the main difference being that [33] assumed a known susceptibility to make the problem linear (using one constant susceptibility for all oceanic crust, and another for all continental crust).

The parameterization must enable a lean forward solution to be computed, in order to retain a feasible computational time in spite of the vast amount of iterations required for the probabilistic inversions. Unfortunately, the amount of model parameters associated with a global nonlinear solution rendered such efforts infeasible. We therefore choose to parameterize an area spanning Greenland and its immediate vicinity in the nonlinear sense, while the remainder of the globe is parameterized in a linear fashion by collapsing the MCT and susceptibility (denoted  $h$  and  $\chi$ , respectively) of each crustal column, into a single unknown Vertically Integrated Magnetization  $VIS = h\chi$ . This allows solving for the contribution from the linear region before the probabilistic inversion is performed. The specific approach taken is thus to first solve a global linear inverse problem for the VIS, and then replace a region encompassing Greenland and its vicinity (the nonlinear region)

with full nonlinear solution. The strength of this approach is that contributions to the total potential (and thus Gauss coefficients), associated with dipoles in the linear region can be recovered prior to a probabilistic inversion. When the probabilistic inversion is then performed, the contribution from the nonlinear region is determined and added to the contribution from the linear region, and the resultant total field is then tested against the data. This approach enables a far more rapid evaluation of each iteration than the global case, while retaining the ability to compute Gauss coefficients and the associated ease of filtering. Furthermore, the approach constrains the amount of prior information required on model parameters, since such information is only strictly necessary in the nonlinear region. As such, the time required to compile this information is greatly reduced. Mathematically, the split-region magnetic potential, as a function of Gauss coefficients, can be expressed through Equations (A1) and (A2):

$$\begin{aligned} g_n^m &\approx \frac{1}{R_\oplus} \left( \frac{R_i}{R_\oplus} \right)^{n+1} \frac{2n+1}{4\pi} \sum_{i=1}^{N_i} (V_{lin}(\mathbf{r}_i) + V_{non}(\mathbf{r}_i)) \cos(m\varphi_i) P_n^m(\cos(\vartheta_i)) d\mathcal{S}_i \\ &= \frac{1}{R_\oplus} \left( \frac{R_i}{R_\oplus} \right)^{n+1} \frac{2n+1}{4\pi} \sum_{i=1}^{N_i} V_{lin}(\mathbf{r}_i) \cos(m\varphi_i) P_n^m(\cos(\vartheta_i)) d\mathcal{S}_i \\ &\quad + \frac{1}{R_\oplus} \left( \frac{R_i}{R_\oplus} \right)^{n+1} \frac{2n+1}{4\pi} \sum_{i=1}^{N_i} V_{non}(\mathbf{r}_i) \cos(m\varphi_i) P_n^m(\cos(\vartheta_i)) d\mathcal{S}_i \end{aligned} \quad (A1)$$

$$\begin{aligned} h_n^m &\approx \frac{1}{R_\oplus} \left( \frac{R_i}{R_\oplus} \right)^{n+1} \frac{2n+1}{4\pi} \sum_{i=1}^{N_i} (V_{lin}(\mathbf{r}_i) + V_{non}(\mathbf{r}_i)) \sin(m\varphi_i) P_n^m(\cos(\vartheta_i)) d\mathcal{S}_i \\ &= \frac{1}{R_\oplus} \left( \frac{R_i}{R_\oplus} \right)^{n+1} \frac{2n+1}{4\pi} \sum_{i=1}^{N_i} V_{lin}(\mathbf{r}_i) \sin(m\varphi_i) P_n^m(\cos(\vartheta_i)) d\mathcal{S}_i \\ &\quad + \frac{1}{R_\oplus} \left( \frac{R_i}{R_\oplus} \right)^{n+1} \frac{2n+1}{4\pi} \sum_{i=1}^{N_i} V_{non}(\mathbf{r}_i) \sin(m\varphi_i) P_n^m(\cos(\vartheta_i)) d\mathcal{S}_i \end{aligned} \quad (A2)$$

where  $V_{lin}(\mathbf{r}_i)$  is the contribution to the magnetic potential from the dipoles in the linear region at all query points  $\mathbf{r}_i$ , and  $V_{non}(\mathbf{r}_i)$  is the contribution to the magnetic potential from dipoles in the nonlinear region at all query points  $\mathbf{r}_i$ . The approximation symbol stems from the numerical summation process replacing integration. In the above equations, it is still necessary to compute the contribution to the global potential from each dipole (in both the linear and nonlinear regions). We therefore limit the contribution from each dipole to a pre-determined region of influence, outside of which those parameters no longer hold any significant influence on the solution. This allows a significant decrease in the computational time required to estimate parameters in the nonlinear region. Simultaneously, it is necessary to ensure a smooth transition between the two regions, such as to avoid unwanted biasing or edge effects. In order to smoothly tie the nonlinear and linear regions together, we form an overlap strategy. The nonlinear region is surrounded by a frame of linear (VIS) tiles to be solved simultaneously with the nonlinear problem. We additionally include data within a 625 km radius outside the outermost VIS tiles, which enforces the transition to be smooth. An overview of the problem parameterization used in the probabilistic inversion is provided as Figure A1.

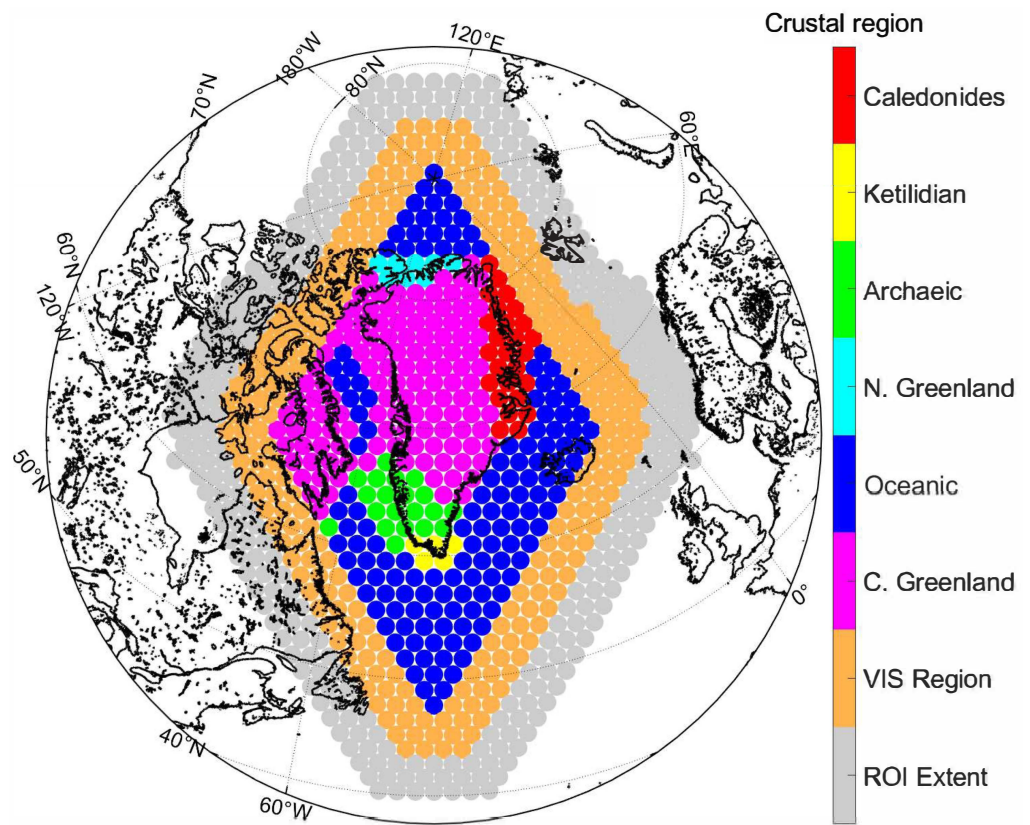


**Figure A1.** Problem parameterization for the probabilistic inversion. Shown are six crustal regions alongside the transition region where a linear problem for vertically integrated susceptibility (VIS) is solved, and the region of influence (ROI) for which data are considered in the nonlinear solution. The ROI and VIS regions are included to avoid edge effects in the transition between nonlinear and linear problem regions. Points within the six crustal regions and the VIS region correspond to crustal column locations (at the surface) and data samples (at satellite altitude), while points in the ROI correspond to data samples only.

#### Appendix A.1. Determining the Distance of Negligible Influence

The distance at which the magnetic field contribution from any point magnetic field source is governed by the fact that  $\mathbf{B}_s \mapsto 0$  as the distance to the source  $d_s \mapsto \infty$ . For a magnetic point-dipole, the magnetic field falls off with the inverse cube of the distance. In geographical spherical coordinates, this can be expressed as in Equation (A3):

$$\mathbf{B}(\mathbf{r}_j, \mathbf{r}_i) \propto \frac{1}{\sqrt{r_i^2 + r_j^2 - 2r_i r_j (\sin(\vartheta_i) \sin(\vartheta_j) \cos(\varphi_i - \varphi_j) + \cos(\vartheta_i) \cos(\vartheta_j))}^3} \quad (\text{A3})$$

where  $\mathbf{B}(\mathbf{r}_j, \mathbf{r}_i)$  is the magnetic field resultant from a dipole at  $\mathbf{r}_j$  measured at  $\mathbf{r}_i$ . A comparison of contributions, relative to the contribution at satellite altitude (300 km), is shown in Table A1.

**Table A1.** Contributions from a crustal dipole to the magnetic field, at various distances. The total distance is the Euclidian distance between a crustal dipole position and a given query point which is always evaluated at satellite altitude, taken as 300 km. The relative impact describes the magnitude of the potential contribution at a given distance from the dipole, relative to that obtained for a query point immediately above it.  $\lambda_{crustmax}$  is the distance corresponding to the wavelength of the lowest spherical harmonic degree ( $n = 16$ ) where the crustal magnetic field is dominant at the surface of the Earth.

Total Distance	Relative Impact	Query Point Position Relative to Dipole
300 km	100%	Immediately above (at satellite altitude)
~625 km	~10.8%	~ $1/4 \lambda_{crustmax}$ away
~1250 km	~1.2%	~ $1/2 \lambda_{crustmax}$ away
~2500 km	~0.16%	~ $\lambda_{crustmax}$ away
~13,000 km	~0.001%	At opposite side of Earth

#### Appendix A.2. Solving the Linear Problem

Determination of contributions from dipoles in the linear region requires multiple steps. To estimate Gauss coefficients, knowledge of either the resultant magnetic potential or resultant magnetic field due to the dipoles in the linear region, is required. We choose to evaluate our inversion using the magnetic field at satellite altitude, due to the scale wavelengths of the crustal dipoles.

Since the contribution from the linear portion of the problem is only to be determined once, the distance of negligible influence can be set relatively high. A cut-off of 2500 km was selected, as this distance corresponds to a low relative contribution, while simultaneously allowing a significant reduction in the amount of matrix elements needed to perform the linear inversion. The choice of 2500 km resulted in a ~95% reduction in the non-zero elements of the system matrix.

We solve the resultant over-determined linear inverse problem for global VIS using the LSQR algorithm [40] for efficient least-squares inversion of sparse matrices. We use a Least-squares inversion with the sole purpose of obtaining a fit that closely mimics the data, in order to preserve the integrity of the dataset for the nonlinear inversion. This is possible since no physical intuition is to be gained from the VIS values; they are simply a mathematical construct with the sole purpose of enabling a lean forward solution for the nonlinear region. In order to provide a truthful representation of the magnetic field, the obtained VIS must result in a magnetic field, where no significant power is contained in spherical harmonic degrees  $1 \leq n \leq 15$ . This is obtained by inverting solely for Gauss coefficients related to spherical harmonic degrees  $n \geq 16$ , and then testing the fit to the expected magnetic field. Since the expected magnetic field only has power in spherical harmonic degrees  $n \geq 16$ , there is no a priori reason to enforce the VIS to reflect otherwise. In order to ensure that the field is sufficiently reproduced in the least squares sense for the defined wavelengths, estimates of misfit are extracted. The highest deviation observed between the VIS-modeled and expected magnetic field was  $<10^{-3}$  nT.

#### Appendix B. Prior Information on the Unknown Model Parameters

A priori information on the MCT of each individual column is available in the form of depth-to-Moho estimates from the tomography-based model of [41] in mainland Greenland, and the CRUST1.0 model of [42] elsewhere. The minimal MCT is set to coincide with the surface. A priori information on Regional Susceptibility (RS) is drawn from the geological subdivision of Greenland and surrounding areas into different macroscopic regions, based on the combined findings of [35–37], with the boundary between continental and oceanic crust adopted from the GPLATES software of [38].

It is assumed that the magnetic susceptibility in each individual region can be described using a single, unknown scalar, leaving one unknown RS value to be determined for each of six different geological regions: Caledonian, Ketilidian, Archaean, Central Greenland, North Greenland, and Oceanic. Due to the scarce susceptibility measurements

available in Greenland, measurements from geologically related regions in Finland, Canada, and Norway were also included as a priori information. Each set of a priori information is associated with an uncertainty, such that each piece of information can be described as a probability density function, which we here assume can be represented as a normal (Gaussian) distribution. This allows a (coarse) initial standard deviation estimate for each RS to be extracted from the compilation of susceptibility measurements. However, the susceptibility samples are in some cases confined to local areas, or contain only a sparse amount of total samples. Furthermore, the susceptibility variation with depth is unknown in most regions. Thus, the possibility of having susceptibility samples that are non-representative of their associated region must be addressed. To account for this, we applied a multi-modeling approach, where several probabilistic models are computed using different a priori uncertainties. We once again stress that the a priori probability distributions are not strictly limiting factors (i.e., not hard constraints). Instead, they should be regarded as general guidelines for the probabilistic solver.

The susceptibility prior is based in a geological subdivision of Greenland, which is obtained by combining the existing sub-division of [36] with the definition of continental crust from the GPLATES software of [38]. The terrane map of [37] (p. 810), is used to extend this subdivision into Canada. This subdivision contains one of the only hard constraints implemented in this study: we assume that the susceptibility of each individual geological region can be described by a single constant, due to its effect being primarily of an induced nature, and measured at sufficient distance. We denote these susceptibility values as the Regional Susceptibilities (RS). The reasoning for this assumption is the availability of prior information on both susceptibility and crustal layout is far too limited for more detailed modeling. Very precise prior models would be required to resolve the strongly nonlinear problem of solving for individual MCT and susceptibility values for each crustal column. Since the currently available data are unable to provide such accuracy, we are forced to make an assumption which will alleviate some of the strongest nonlinearity. We choose to do this through RS, since a geologically founded argument can be made about similar geological regions most likely having overall similar properties, and thus similar magnetic susceptibilities. An overview of the compiled susceptibility information is presented in Table A2.

**Table A2.** Overview of compiled prior information on Regional Susceptibilities.

Region	Upper Crust Susceptibility	Lower Crust Susceptibility	Data Type
Ketilidian	$1.783 \times 10^{-3}$	$16.4 \times 10^{-3}$ or $35 \times 10^{-3}$	Inferred
Archaean	$14.1 \times 10^{-3} \pm 10.6 \times 10^{-3}$ or $30 \times 10^{-3}$	$35 \times 10^{-3}$	Inferred
Caledonian	$8.3 \times 10^{-3}$	N/A	Direct
Central	$7.8 \times 10^{-3}$	$35 \times 10^{-3}$	Inferred
North	$19.3 \times 10^{-3}$	N/A	Inferred
oceanic	$40 \times 10^{-3}$	N/A	Inferred

### Appendix B.1. Susceptibility as a Function of Depth and Temperature

The results of [54] suggest that magnetic susceptibilities in the lower crust may exceed that of the upper crust, finding an average susceptibility of  $35 \times 10^{-3}$  based on 4435 samples across 255 sites from Lofoten and Vesterålen, in Norway. Interestingly, they also find that some representative samples from those regions show a constant or slightly increasing susceptibility with increasing temperature, before dropping sharply to zero immediately prior to reaching the Curie temperature of magnetite. Wherever susceptibility information for lower crust was available, the values for upper and lower crust were averaged, in order to obtain the mean prior susceptibility for the corresponding crustal region. The mean prior susceptibility values were also varied across the different modeling runs, as described in Appendix D. This variation included disregarding the susceptibility information in the deeper crust.

### *Appendix B.2. Susceptibility of the Ketilidian Mobile Belt*

Prior information on Ketilidian RS was constructed from measurements from the Svecofennian region, based on the suggestion of [44] that crust in the Ketilidian fold belt and the Svecofennian region are similar. Susceptibility measurements on a series of Svecofennian rocks in Finland are provided in [49]. For the Ketilidian prior, we use only susceptibility data from host rocks (varying in composition from quartz diorite to gabbro). This yields a mean Ketilidian upper susceptibility of  $1.783 \times 10^{-3}$ .

The authors of [60] (p. 216) stated that the results of the Ketilidian orogeny visible in the Makkovik region are visible as reworked Archaean basement from the Nain Province immediately north of the Makkovik Province, but both [45,59] (p. 135) suggested that the Ketilidian fold belt region has no underlying Archaean crust. As such, information is unclear on whether or not to include deeper Archaean crust in this prior. The authors of [55] found a mean susceptibility value for Ahvenisto gabbro-anorthosites in southeast Finland of  $16.4 \times 10^{-3}$ , which could suggest that this value may be suitable for the deeper part of the Ketilidian Mobile Belt.

### *Appendix B.3. Susceptibility of the Archaean Block*

Prior information on RS of the Archaean Block is drawn from available data from the Archaean crust in the Superior Province in Manitoba, Canada. The authors of [56] obtained a modified mean susceptibility estimate of  $14.1 \times 10^{-3} \pm 10.6 \times 10^{-3}$  for silicic gneisses and intrusive rocks ([56] (p. 178)). The authors of [57] obtained a mean susceptibility of  $\sim 0.03$  for an area roughly comprising the northeast of the superior province, while also demonstrating the small length scales of variation for crustal susceptibility. For the lower Archaean crust, the findings of [54] suggest a susceptibility of  $35 \times 10^{-3}$ .

### *Appendix B.4. Susceptibility of the Caledonian Fold Belt*

Prior information on RS in the Greenlandic Caledonides is available as both in situ measurements and through inference from studies of the Norwegian Caledonides. There is some evidence that the Caledonides overlay deeper Precambrian rocks [46,51], and thus, we seek susceptibility data from both Caledonides and underlying Precambrian igneous rocks.

In [52], the authors performed 3330 susceptibility measurements, collected across 102 individual localities within the Caledonian fold belt region in Greenland. Susceptibilities are given per location, with the mean susceptibility of basement gneisses and basement amphibolites across all locations being  $8.3 \times 10^{-3}$  (giving equal weight to each location).

Interestingly, this correlates well to susceptibility values from [51], which includes well-distributed samples along the coast of Norway. By excluding the measurements of basement norite found outside the Norwegian Caledonides in the Tellnes, Rogaland region, a mean susceptibility of  $7 \times 10^{-3}$  for the Norwegian Caledonides is obtained.

### *Appendix B.5. Susceptibility of the Central Region*

The authors of [59] (p. 135) concluded that the Rinkian fold belt in the western part of the Central region is generally comprised of a reworked Early Proterozoic cover, underlain by reworked Archaean crystalline infrastructure. The existence of Archaean crust within the central region is also suggested by [47], who found an unworked Archaean basement in northeastern Disko Bugt.

The authors of [48] expected some relation between crust in the central region and that of Baffin island. A few susceptibility measurements from Nunavut territory, Canada, in southern Baffin Island is provided by [50], from which we obtain an average value of  $7.8 \times 10^{-3}$ .

### *Appendix B.6. Susceptibility of the North Greenland Fold Belt*

The geological divisions of [36] (Chap. 1, p. 32) and [43] (p. 218) agree that the North Greenland Fold Belt and the northern part of Ellesmere Island are correlated. We therefore assume that their susceptibilities are comparable. Susceptibility measurements from the Yelverton Bay area in northern Ellesmere Island are presented in [53], through which we deduce a mean susceptibility estimate of  $19.3 \times 10^{-3}$ .

### *Appendix B.7. Susceptibility of the Oceanic crust*

Determination of a single susceptibility for Oceanic crust is challenging, especially in the global perspective. The authors of [33] employed a constant susceptibility value of  $40 \times 10^{-3}$  for oceanic crust globally, following [58,61]. We here adopt this value as the mean.

## **Appendix C. Probabilistic Solution Process and Forward Modeling Equations**

We use the Solution to Inverse Problems with complex Prior Information (SIPPI) framework of [25,26], which is based on the Markov-Chain Monte Carlo Metropolis Algorithm, see [24]. In the forward solver of the probabilistic solution process, we also perform a number of necessary transformations. The general flow of the probabilistic solver is:

1. Construct suitable probability distributions of the available prior information;
2. Draw a realization for each model parameter from the prior information;
3. Filter the model response to the same wavelengths as the crustal data (via Gauss Coefficients);
4. Solve the forward problem to obtain the magnetic response of the model, and compute the data misfit;
5. Evaluate whether or not to take a step in model space;
6. Repeat this process starting from step 2.

### *Appendix C.1. Sampling Strategy*

SIPPI [25,26] provides numerous options with regard to sampling the posterior. The main features relevant to our use case are:

1. Simulated annealing, in particular its ability to initialize the sampling scheme using a specific exploration setting, and then gradually decreasing that level of exploration;
2. Sequential Gibbs sampling, which enables us to optimize the step sizes taken toward a specific accept/reject rate;
3. Perturbation strategy, in particular how many parameter should be perturbed per iteration;
4. Iterations between posterior realizations, which enables us to determine how many iterations must occur before realizations can be considered statistically independent.

Since a full modeling run is computationally expensive, these parameters and the initial sampler convergence/burn-in rate (initial iterations required to progress from the initially drawn prior realization to a local/potential solution), are initially optimized using down-scaled modeling runs. Initial testing provided estimates of burn-in rate in the range of  $4 \times 10^4$  and  $8 \times 10^4$  iterations. We therefore suggest a minimal initial burn-in rate of  $10^5$  iterations before posterior samples can be drawn. The temperature (exploration parameter) during simulated annealing was found to have little effect on the output unless set exceptionally high ( $\leq 1000$  times the standard value), in which case some slight alterations in the structure occurred (but note that regardless of configuration, the vast majority of general structures in the output models remained the same in all tests performed). The use of simulated annealing imposes some requirements for sequential Gibbs sampling, as the final step length (determined at the last Gibbs iterations) should be optimized using the final temperature, unless an artificially large step length is desired in the solution (we utilize this for robustness tests). Note that no posterior samples can be drawn for the a posteriori probability density function before both burn-in, simulated annealing, and sequential Gibbs sampling have all been completed.

Due to the sheer volume of priors, the perhaps most challenging parameter to determine is the amount of iterations between independent realizations of the posterior. The distance between independent realizations is diminished when increasing sampling temperature, as a trade-off with how strict the rejection of prior realizations solutions by the sampler. Setting the temperature too high may result in re-sampling the prior, while a too low temperature may result in posterior realizations being dependent. The video method of [23] was employed as a general guideline to evaluate the independence of the drawn realizations. For the main modeling runs, where the largest amount of realizations could be drawn, we also compare downsampled subsets of the posterior pdf (with samples drawn further apart) to evaluate any potential change in the posterior pdf. Both of these tests suggested that the posterior realizations generally having some degree of independence, with high-temperature, high-uncertainty models having the largest degrees of independence in the posterior, and vice versa.

### Appendix C.2. Forward Modeling Equations

The equations relevant to the forward problem are provided in the following, in the same flow order as they are used in the probabilistic solver. First, the Gauss coefficients associated with the current prior realization are computed. These are obtained by computing the term for the nonlinear region in Equations (A1) and (A2), with the magnetic potential of the parameterization obtained as in Equation (A4):

$$V(\mathbf{r}_i) = \frac{\mu_0}{4\pi} \sum_{\text{all } \mathbf{r}_j} \mathbf{j}(\mathbf{r}_j) \cdot \nabla_j |\mathbf{r}_i - \mathbf{r}_j|^{-1} \quad (\text{A4})$$

where  $\mathbf{r}_i = (r_i, \vartheta_i, \varphi_i)$  is the position of the  $i$ -th query point (data sample location),  $\mu_0 = 4\pi \times 10^{-7} [\frac{N}{A^2}]$ ,  $N \in \mathbb{N}$  is the amount of crustal dipoles,  $\nabla_j$  is the spherical gradient operator acting on the the individual elements of the position of the  $j$ -th dipole,  $\mathbf{r}_j = (r_j, \vartheta_j, \varphi_j)$ , and  $\mathbf{j}(\mathbf{r}_j) = (j_r(\mathbf{r}_j), j_\vartheta(\mathbf{r}_j), j_\varphi(\mathbf{r}_j))$  is the magnetic dipole moment of the dipole located at  $\mathbf{r}_j$ . We refer the interested reader to [34] for details and explicit equations related to the ESMD method.

Having obtained the Gauss coefficients, they are used to filter the response to the considered crustal wavelengths, defined as all spherical harmonic degree  $16 \leq n \leq 80$ . The retained Gauss coefficients are then converted to vector magnetic field components through Equation (A5):

$$\mathbf{B}(\mathbf{r}) = -\nabla \left[ R_\oplus \sum_n^N \sum_m^n \left( \frac{R_\oplus}{r} \right)^{n+1} \left( g_n^m \cos(m\varphi) + h_n^m \sin(m\varphi) \right) P_n^m \right] \quad (\text{A5})$$

where  $\nabla$  is the spherical gradient operator,  $R_\oplus \approx 6371$  km is the Earth's mean radius,  $n$  and  $m$  are spherical harmonic degree and order, respectively, and  $P_n^m = P_n^m(\cos \vartheta)$  is the corresponding Schmidt-normalized Legendre function for degree and order  $n$  and  $m$ .

In order to maximize efficiency, we precompute all terms and partial terms of the equations which do not vary during the computations, and vectorize the remaining computations.

### Appendix D. Modeling Runs, Modeling Results, and GTHF Estimation

Figure 4 of the main text includes mean posterior MCT models of eight different modeling runs. Runs II and III were constructed from available data, using either an assumption of increasing susceptibility with depth (II) or solely susceptibility values of which evidence has been presented (III), i.e., only the susceptibility prior is perturbed in runs II and III. The remaining runs seek to stress-test the modeling output by further perturbation, such as by imposing assumption on the accuracy of the input information (both in the sense of having more and/or less accurate information). An overview of the differences between the eight secondary runs is provided here, while explicit parameter values associated with the runs are shown in Tables A3 and A4.

- II. Lower susceptibility of 35 assumed in the absence of lower susceptibility data;
- III. Strictly using the information available (no increase in susceptibility with depth without some form of geological evidence);
- IV. Same as III, but with a few of the susceptibility priors assumed to be more accurate than others, i.e., a few are assumed to already represent the RS well;
- V. Same as III, but with all of the susceptibility priors assumed to be more accurate, i.e., assumed to be good representations of the RS, and the data assumed to be less certain. The ocean floor MCT was also assumed to be even more uncertain than usual;
- VI. Same as II, but with a less certain MCT estimate alongside a less certain susceptibility estimate, while the data are assumed to be more accurate;
- VII. Same as II, but with a less certain MCT estimate while the data are assumed to be more accurate;
- VIII. Same as II, but with a less certain MCT estimate while, less certain data, and a higher overall susceptibility in the continental crust (the mean susceptibility values used to seed this run are equivalent to the fixed values used in [17]);
- IX. Same as II, but with more uncertain MCT estimates, more uncertain susceptibilities, and more uncertain data.

**Table A3.** Prior model parameter values applied in the inversion. Means for crustal MCT (C-MCT) and oceanic MCT (O-MCT) are given as fractions of the models used to predict their maximum extent. Susceptibility means are given in SI units [ $\times 10^{-3}$ ]. All prior standard deviations are given as fractions of their means.

		Ia	Ib	II	III	IV	V	VI	VII	VIII	IX
Mean	C-MCT	3/4	3/4	3/4	3/4	3/4	3/4	2/3	2/3	2/3	2/3
	O-MCT	1/2	1/2	1/2	1/2	1/2	1/2	2/3	2/3	2/3	2/3
	VIS	0.04	0.04	0.04	0.04	0.04	0.04	0.04	0.04	0.04	0.04
	Ketilidian	9.1	9.1	9.1	9.1	9.1	9.1	9.1	9.1	35.0	9.1
	Archaean	24.6	24.6	24.6	14.1	14.1	14.1	24.6	24.6	35.0	24.6
	Caledonian	21.7	21.7	21.7	8.3	8.3	8.3	21.7	21.7	35.0	21.7
	Central	21.4	21.4	21.4	7.8	7.8	7.8	21.4	21.4	35.0	21.4
	North	27.2	27.2	27.2	19.3	19.3	19.3	27.2	27.2	35.0	27.2
	Oceanic	40.0	40.0	40.0	40.0	40.0	40.0	40.0	40.0	40.0	40.0
$\sigma$	C-MCT	1/8	1/8	1/8	1/8	1/8	1/8	1/5	1/6	1/5	1/5
	O-MCT	1/4	1/4	1/4	1/4	1/4	1/2	1/5	1/6	1/5	1/5
	VIS	1/3	1/3	1/3	1/3	1/3	1/3	1/3	1/3	1/3	1/3
	Ketilidian	1/3	1/3	1/3	1/3	1/6	1/6	1/2	1/3	1/3	1/2
	Archaean	1/3	1/3	1/3	1/3	1/6	1/6	1/2	1/3	1/3	1/2
	Caledonian	1/3	1/3	1/3	1/3	1/3	1/6	1/2	1/3	1/3	1/2
	Central	1/3	1/3	1/3	1/3	1/3	1/6	1/2	1/3	1/3	1/2
	North	1/3	1/3	1/3	1/3	1/3	1/6	1/2	1/3	1/3	1/2
	Oceanic	1/3	1/3	1/3	1/3	1/3	1/6	1/2	1/3	1/3	1/2

**Table A4.** Modeling parameters and prior data distribution parameters employed in each inversion run. \* Data outside the VIS region (but inside the ROI region) were assigned a standard deviation of 5 nT for run Ia.

		Ia	Ib	II	III	IV	V	VI	VII	VIII	IX
$N_{samp}$	BurnIn	$1 \times 10^6$									
	Seq.Gibbs	$1 \times 10^3$	$1 \times 10^4$	$1 \times 10^3$							
	$N_{posterior}$	700	700	99	94	100	100	100	100	100	100

**Table A4.** *Cont.*

		Ia	Ib	II	III	IV	V	VI	VII	VIII	IX
$\delta_{post}$		$1 \times 10^4$	$1 \times 10^4$	$2 \times 10^4$							
SimAnneal	0		$1 \times 10^3$	$5 \times 10^5$							
$T$	SimAnneal	1	100	5	5	5	5	5	5	5	5
	Sampling	1	3	1	1	1	1	1	1	1	1
$\sigma$ [nT]	Data	1 *	1	1	1	1	1.7	0.5	0.5	1.7	1.5

#### Appendix D.1. Susceptibility Results

The susceptibility results associated with the ten different modeling runs are provided in Table A5.

**Table A5.** Posterior mean and standard deviations for the different RS results. All susceptibility means and standard deviations are given in SI units [ $\times 10^{-3}$ ]. Apart from some variance across runs in the Ketilidian and Achaean RS, the RS posteriors correlate well for the numbered runs, regardless of the specific prior supplied. Recall that an assumption of purely induced dipole moments, directed along the core magnetic field, was imposed for all columns. As such, the susceptibilities may deviate from actual crustal properties, and especially so in regions with strong remnant magnetization. However, apart from the significantly increased Oceanic susceptibility, which is expected to stem from the model driving the oceanic MCT to near zero, the susceptibilities still generally fall within reasonable bounds.

		Ia	Ib	II	III	IV	V	VI	VII	VIII	IX
Mean	Ketilidian	18.1	22.5	45.4	45.9	30.5	21.2	60.0	45.4	78.9	51.1
	Archaean	95.7	81.5	62.8	58.4	44.3	42.6	76.8	65.3	78.5	75.4
	Caledonian	35.7	21.3	19.9	18.5	14.5	11.0	24.9	25.2	28.4	25.7
	Central	60.2	42.9	35.9	33.9	28.3	26.4	39.1	38.7	45.4	42.3
	North	25.2	8.7	9.4	5.4	7.9	7.9	8.1	12.0	14.2	12.9
	Oceanic	39.1	40.9	76.9	74.3	58.8	63.0	56.2	45.9	55.7	54.2
$\sigma$	Ketilidian	1.0	2.4	1.4	0.8	0.4	1.1	0.7	0.5	4.8	2.1
	Archaean	2.8	2.6	1.4	1.0	0.6	1.3	1.9	0.4	3.4	3.0
	Caledonian	0.9	1.4	0.8	0.4	0.4	0.7	0.4	0.5	1.7	1.5
	Central	1.0	1.2	0.5	0.4	0.2	0.5	0.4	0.2	1.3	1.0
	North	1.9	2.0	0.7	0.9	0.6	1.7	0.6	0.9	3.3	2.4
	Oceanic	3.1	13.6	1.4	2.4	1.3	3.2	0.2	0.5	1.9	2.1

#### Appendix D.2. Estimating Geothermal Heat Flux

In order to estimate the Geothermal heat flux, a thermal model of the crust is required. The thermal model should account for the thermal conductivity throughout the crust, as well as any additional heat sources present, such as decaying radioisotopes, as suggested by [67]. As such, our GTHF estimates are based on a one-dimensional solution of the Heat equation with an internal heat production term:

$$\rho C_p \frac{\partial u}{\partial t} = \nabla \cdot k \nabla u + q \quad (\text{A6})$$

where  $u = u(t, \mathbf{p})$  is the temperature,  $\mathbf{p}$  is the position vector in the chosen coordinate system,  $k$  is the thermal conductivity,  $\rho$  is the density,  $C_p$  is the specific heat capacity, and  $q = q(t, \mathbf{p})$  is the internal source term. We assume that the crust is in a steady thermal state.

A classical approach is to employ a one-dimensional thermal model, assuming that thermal conductivity is constant throughout a number of layers, and that the internal heat production varies with depth in either a linear or exponential manner. However,

the authors of [66] suggested that neither of these classical models of heat production are accurate, while [68] suggested that the exponential model should be abandoned altogether. The results of [69] cast further light on the non-trivial nature of the crustal heat production. Left with no obvious choice for a crustal model, we follow the approach taken by [17,64], using an exponential heat production model. Due to the vast uncertainties surrounding the crustal heat production, we consider an overly complex thermal conductivity model to be unwarranted, and therefore employ a single layer conductivity model:

$$q(z) = q_0 \exp\left(-\frac{z}{D}\right) \quad (\text{A7})$$

where  $q_0$  is a constant specifying the heat production at the top of the upper crust, and  $D$  is the scale depth at which  $q(z) = q_0 \exp(-1)$ . The solution to the resultant boundary value problem to determine surface GTHF is

$$q_{\text{surface}} = -Dq_0 - \frac{u_c - u_0}{z_c} k - \frac{D^2 q_0}{z_c} \left( \exp\left(-\frac{z_c}{D}\right) - 1 \right) \quad (\text{A8})$$

where  $z_c$  is the depth to the Curie isotherm (also known as the MCT),  $u_c$  is the Curie temperature of the crust, and  $u_0$  is the temperature of the surface of the crust. In order to solve the one-dimensional heat equation for the surface heat flux using the posterior MCT, a temperature bound at the base of the magnetic crust required. The authors of [17,33] assumed that the Curie point of the crust equals that of Magnetite, yielding a lower temperature bound of  $\sim 580$  °C. However, [54] found single Curie points from a representative selection of magnetite bearing rocks between  $\sim 550$  °C and  $\sim 575$  °C. This is supported by [56], where the susceptibility of magnetite-bearing samples was found to drop off sharply from around  $\sim 540$  °C, towards the Curie point at  $\sim 580$  °C. These studies suggest a lower temperature boundary between  $\sim 550$  °C to  $\sim 570$  °C, of which we adopt the higher as the effective temperature boundary at the base of the magnetic crust. For the constants, the values of  $D = 8$  km,  $q_0 = 2.5 \times 10^{-6}$ ,  $\frac{\text{W}}{\text{m}^3}$ , and the choice of  $k = 2.4$   $\frac{\text{W}}{\text{K m}}$  are adopted from [65].

## References

1. Wolfe, C.J.; Bjarnason, I.T.; VanDecar, J.C.; Solomon, S.C. Seismic structure of the Iceland mantle plume. *Nature* **1997**, *385*, 245–247. [\[CrossRef\]](#)
2. Bijwaard, H.; Spakman, W. Tomographic evidence for a narrow whole mantle plume below Iceland. *Earth Planet. Sci. Lett.* **1999**, *166*, 121–126. [\[CrossRef\]](#)
3. French, S.W.; Romanowicz, B. Broad plumes rooted at the base of the Earth's mantle beneath major hotspots. *Nature* **2015**, *525*, 95–99. [\[CrossRef\]](#) [\[PubMed\]](#)
4. Anell, I.; Thybo, H.; Artemieva, I.M. Cenozoic uplift and subsidence in the North Atlantic region: Geological evidence revisited. *Tectonophysics* **2009**, *474*, 78–105. [\[CrossRef\]](#)
5. Bonow, J.M.; Japsen, P.; Nielsen, T.F. High-level landscapes along the margin of southern East Greenland—A record of tectonic uplift and incision after breakup in the NE Atlantic. *Glob. Planet. Chang.* **2014**, *116*, 10–29. [\[CrossRef\]](#)
6. Døssing, A.; Japsen, P.; Watts, A.B.; Nielsen, T.; Jokat, W.; Thybo, H.; Dahl-Jensen, T. Miocene uplift of the NE Greenland margin linked to plate tectonics: Seismic evidence from the Greenland Fracture Zone, NE Atlantic. *Tectonics* **2016**, *35*, 257–282. [\[CrossRef\]](#)
7. Rohrman, M.; van der Beek, P. Cenozoic postrift domal uplift of North Atlantic margins: An asthenospheric diapirism model. *Geology* **1996**, *24*, 901–904. [\[CrossRef\]](#)
8. Arrowsmith, S.J.; Kendall, M.; White, N.; VanDecar, J.C.; Booth, D.C. Seismic imaging of a hot upwelling beneath the British Isles. *Geology* **2005**, *33*, 345–348. [\[CrossRef\]](#)
9. Rickers, F.; Fichtner, A.; Trampert, J. The Iceland–Jan Mayen plume system and its impact on mantle dynamics in the North Atlantic region: Evidence from full-waveform inversion. *Earth Planet. Sci. Lett.* **2013**, *367*, 39–51. [\[CrossRef\]](#)
10. Steinberger, B.; Bredow, E.; Lebedev, S.; Schaeffer, A.; Torsvik, T.H. Widespread volcanism in the Greenland–North Atlantic region explained by the Iceland plume. *Nat. Geosci.* **2019**, *12*, 61–68. [\[CrossRef\]](#)
11. Torsvik, T.H.; Mosar, J.; Eide, E.A. Cretaceous–tertiary geodynamics: A North Atlantic exercise. *Geophys. J. Int.* **2001**, *146*, 850–866. [\[CrossRef\]](#)
12. Forsyth, D.A.; Morel-AL'Huissier, P.; Asudeh, I.; Green, A.G. Alpha Ridge and iceland-products of the same plume? *J. Geodyn.* **1986**, *6*, 197–214. [\[CrossRef\]](#)
13. Lawver, L.A.; Müller, R.D. Iceland hotspot track. *Geology* **1994**, *22*, 311–314. [\[CrossRef\]](#)

14. Steinberger, B.; Spakman, W.; Japsen, P.; Torsvik, T.H. The key role of global solid-Earth processes in preconditioning Greenland's glaciation since the Pliocene. *Terra Nova* **2015**, *27*, 1–8. [[CrossRef](#)]
15. Smith-Johnsen, S.; de Fleurian, B.; Schlegel, N.; Seroussi, H.; Nisancioglu, K. Exceptionally high heat flux needed to sustain the Northeast Greenland Ice Stream. *Cryosphere* **2020**, *14*, 841–854. [[CrossRef](#)]
16. Khan, S.; Choi, Y.; Morlighem, M.; Rignot, E.; Helm, V.; Humbert, A.; Mouginot, J.; Millan, R.; Kjær, K.; Bjørk, A. Extensive inland thinning and speed-up of Northeast Greenland Ice Stream. *Nature* **2022**, *611*, 727–732. [[CrossRef](#)]
17. Fox Maule, C.; Purucker, M.E.; Olsen, N. *Inferring magnetic Crustal Thickness and Geothermal Heat Flux from Crustal Magnetic Field Models*. Danish Climate Centre, Report 09–09; Danish Meteorological Institute: Copenhagen, Denmark, 2009.
18. Martos, Y.M.; Jordan, T.A.; Catalán, M.; Jordan, T.M.; Bamber, J.L.; Vaughan, D.G. Geothermal Heat Flux Reveals the Iceland Hotspot Track Underneath Greenland. *Geophys. Res. Lett.* **2018**, *45*, 8214–8222. [[CrossRef](#)]
19. Greve, R. Relation of measured basal temperatures and the spatial distribution of the geothermal heat flux for the Greenland ice sheet. *Ann. Glaciol.* **2005**, *42*, 424–432. [[CrossRef](#)]
20. Colgan, W.; Wansing, A.; Mankoff, K.; Lösing, M.; Hopper, J.; Loudon, K.; Ebbing, J.; Christiansen, F.G.; Ingeman-Nielsen, T.; Liljedahl, L.C.; et al. Greenland Geothermal Heat Flow Database and Map (Version 1). *Earth Syst. Sci. Data* **2022**, *14*, 2209–2238. [[CrossRef](#)]
21. Rogozhina, I.; Hagedoorn, J.M.; Martinec, Z.; Fleming, K.; Soucek, O.; Greve, R.; Thomas, M. Effects of uncertainties in the geothermal heat flux distribution on the Greenland Ice Sheet: An assessment of existing heat flow models. *J. Geophys. Res. Earth Surf.* **2012**, *117*, F02025. [[CrossRef](#)]
22. Bamber, J.L.; Layberry, R.L.; Gogineni, S. A new ice thickness and bed data set for the Greenland ice sheet: 1. Measurement, data reduction, and errors. *J. Geophys. Res. Atmos.* **2001**, *106*, 33773–33780. [[CrossRef](#)]
23. Tarantola, A. *Inverse Problem Theory and Methods for Model Parameter Estimation*; SIAM: Philadelphia, PA, USA, 2005; p. 342.
24. Mosegaard, K.; Tarantola, A. Monte Carlo sampling of solutions to inverse problems. *J. Geophys. Res. Solid Earth* **1995**, *100*, 12431–12447. [[CrossRef](#)]
25. Hansen, T.M.; Cordua, K.S.; Looms, M.C.; Mosegaard, K. SIPPI: A Matlab toolbox for sampling the solution to inverse problems with complex prior information: Part 1—Methodology. *Comput. Geosci.* **2013**, *52*, 470–480. [[CrossRef](#)]
26. Hansen, T.M.; Cordua, K.S.; Looms, M.C.; Mosegaard, K. SIPPI: A Matlab toolbox for sampling the solution to inverse problems with complex prior information: Part 2—Application to crosshole GPR tomography. *Comput. Geosci.* **2013**, *52*, 481–492. [[CrossRef](#)]
27. Steinberger, B.; Sutherland, R.; O'Connell, R.J. Prediction of Emperor-Hawaii seamount locations from a revised model of global plate motion and mantle flow. *Nature* **2004**, *430*, 167–173. [[CrossRef](#)]
28. Cox, A.; Hart, R.B. *Plate Tectonics: How It Works*; John Wiley & Sons: Hoboken, NJ, USA, 2009.
29. O'Neill, C.; Müller, D.; Steinberger, B. On the uncertainties in hot spot reconstructions and the significance of moving hot spot reference frames. *Geochem. Geophys. Geosystems* **2005**, *6*. [[CrossRef](#)]
30. Doubrovine, P.V.; Steinberger, B.; Torsvik, T.H. Absolute plate motions in a reference frame defined by moving hot spots in the Pacific, Atlantic, and Indian oceans. *J. Geophys. Res. Solid Earth* **2012**, *117*. [[CrossRef](#)]
31. Müller, R.D.; Royer, J.Y.; Lawver, L.A. Revised plate motions relative to the hotspots from combined Atlantic and Indian Ocean hotspot tracks. *Geology* **1993**, *21*, 275–278. [[CrossRef](#)]
32. Olsen, N.; Ravat, D.; Finlay, C.; Kother, L.K. LCS-1: A high-resolution global model of the lithospheric magnetic field derived from CHAMP and Swarm satellite observations. *Geophys. J. Int.* **2017**, *211*, 1461–1477. [[CrossRef](#)]
33. Fox Maule, C.; Purucker, M.E.; Olsen, N.; Mosegaard, K. Heat flux anomalies in Antarctica revealed by satellite magnetic data. *Science* **2005**, *309*, 464–467. [[CrossRef](#)] [[PubMed](#)]
34. Dyment, J.; Arkani-Hamed, J. Equivalent source magnetic dipoles revisited. *Geophys. Res. Lett.* **1998**, *25*, 2003–2006. [[CrossRef](#)]
35. Escher, A.; Watt, W.S. *Geology of Greenland*; Geological Survey of Greenland: København, Denmark, 1976.
36. Goodwin, A.M. Chapter 1—Distribution and Tectonic Setting of Precambrian Crust. In *Principles of Precambrian Geology*; Goodwin, A.M., Ed.; Academic Press: London, UK, 1996; p. 32. [[CrossRef](#)]
37. Kolb, J. Structure of the Palaeoproterozoic Nagssugtoqidian Orogen, South-East Greenland: Model for the tectonic evolution. *Precambrian Res.* **2014**, *255*, 809–822. [[CrossRef](#)]
38. Matthews, K.J.; Maloney, K.T.; Zahirovic, S.; Williams, S.E.; Seton, M.; Mueller, R.D. Global plate boundary evolution and kinematics since the late Paleozoic. *Glob. Planet. Chang.* **2016**, *146*, 226–250. [[CrossRef](#)]
39. Tarantola, A.; Valette, B. Inverse Problems = Quest for Information. *J. Geophys.* **1982**, *50*, 159–170.
40. Paige, C.; Saunders, M. LSQR—An algorithm for sparse linear-equations and sparse least-squares. *ACM Trans. Math. Softw.* **1982**, *8*, 43–71. [[CrossRef](#)]
41. Darbyshire, F.A.; Dahl-Jensen, T.; Larsen, T.B.; Voss, P.H.; Joyal, G. Crust and uppermost-mantle structure of Greenland and the Northwest Atlantic from Rayleigh wave group velocity tomography. *Geophys. J. Int.* **2018**, *212*, 1546–1569. [[CrossRef](#)]
42. Laske, G.; Masters, G.; Ma, Z.; Pasyanos, M. Update on CRUST1.0—A 1-degree Global Model of Earth's Crust. In Proceedings of the EGU General Assembly Conference Abstracts, Gottingen, Germany, 23–28 April 2013; Volume 15, p. EGU2013-2658.
43. St-Onge, M.R.; Van Gool, J.A.; Garde, A.A.; Scott, D.J. Correlation of Archaean and Palaeoproterozoic units between northeastern Canada and western Greenland: Constraining the pre-collisional upper plate accretionary history of the Trans-Hudson orogen. *Geol. Soc.* **2009**, *318*, 193–235. [[CrossRef](#)]

44. Kerr, A.; Hall, J.; Wardle, R.; Gower, C.; Ryan, B. New reflections on the structure and evolution of the Makkovikian-Ketilidian Orogen in Labrador and southern Greenland. *Tectonics* **1997**, *16*, 942–965. [[CrossRef](#)]
45. Van Breemen, O.; Aftalion, M.; Allaart, J. Isotopic and geochronologic studies on granites from the Ketilidian mobile belt of South Greenland. *Geol. Soc. Am. Bull.* **1974**, *85*, 403–412. [[CrossRef](#)]
46. Korja, T.; Smirnov, M.; Pedersen, L.B.; Gharibi, M. Structure of the Central Scandinavian Caledonides and the underlying Precambrian basement, new constraints from magnetotellurics. *Geophys. J. Int.* **2008**, *175*, 55–69. [[CrossRef](#)]
47. Kalsbeek, F.; Taylor, P.; Pidgeon, R. Unreworked Archean Basement and Proterozoic Supracrustal Rocks from Northeastern Disko Bugt, West Greenland—Implications for the Nature of Proterozoic Mobile Belts in Greenland. *Can. J. Earth Sci.* **1988**, *25*, 773–782. [[CrossRef](#)]
48. Sanborn-Barrie, M.; Thrane, K.; Wodicka, N.; Rayner, N. The Laurentia—West Greenland connection at 1.9 Ga: New insights from the Rinkian fold belt. *Gondwana Res.* **2017**, *51*, 289–309. [[CrossRef](#)]
49. Mertanen, S.; Karell, F. Rock magnetic investigations constraining relative timing for gold deposits in Finland. *Bull. Geol. Soc. Finl.* **2011**, *83*, 75–94. [[CrossRef](#)]
50. Tschirhart, V.; St-Onge, M.R.; Weller, O. Preliminary geophysical interpretation of the McKeand River area, southern Baffin Island, Nunavut: Insights from gravity, magnetic and geological data. *Summ. Act.* **2015**, *2015*, 49–60.
51. Olesen, O.; Bronner, M.; Ebbing, J.; Gellein, J.; Gernigon, L.; Koziel, J.; Lauritsen, T.; Myklebust, R.; Pascal, C.; Sand, M.; et al. New aeromagnetic and gravity compilations from Norway and adjacent areas: Methods and applications. *Pet. Geol. Conf. Ser.* **2010**, *7*, 559–586. [[CrossRef](#)]
52. Schlindwein, V. Structure and evolution of the continental crust of northern east Greenland from integrated geophysical studies. *Ber. Polarforsch.* **1998**, *270*, 15227–15245. [[CrossRef](#)]
53. Estrada, S.; Damaske, D.; Henjes-Kunst, F.; Schreckenberger, B.; Oakey, G.N.; Piepjohn, K.; Eckelmann, K.; Linnemann, U. Multistage Cretaceous magmatism in the northern coastal region of Ellesmere Island and its relation to the formation of Alpha Ridge—Evidence from aeromagnetic, geochemical and geochronological data. *Nor. J. Geol.* **2016**, *96*, 65–95. [[CrossRef](#)]
54. Schlinger, C.M. Magnetization of lower crust and interpretation of regional magnetic anomalies: Example from Lofoten and Vesteralen, Norway. *J. Geophys. Res.* **1985**, *90*, 11484–11504. [[CrossRef](#)]
55. Elo, S.; Korja, A. Geophysical Interpretation of the Crustal and Upper-Mantle Structure in the Wiboorg Rapakivi Granite Area, Southeastern Finland. *Precambrian Res.* **1993**, *64*, 273–288. [[CrossRef](#)]
56. Williams, M.; Shive, P.; Fountain, D.; Frost, B. Magnetic-Properties of Exposed Deep crustal Rocks From the Superior Province of Manitoba. *Earth Planet. Sci. Lett.* **1985**, *76*, 176–184. [[CrossRef](#)]
57. Pilkington, M.; Percival, J.A. Crustal magnetization and long-wavelength aeromagnetic anomalies of the Minto block, Quebec. *J. Geophys. Res. Solid Earth* **1999**, *104*, 7513–7526. [[CrossRef](#)]
58. Purucker, M.; Langlais, B.; Olsen, N.; Hulot, G.; Mandea, M. The southern edge of cratonic North America: Evidence from new satellite magnetometer observations. *Geophys. Res. Lett.* **2002**, *29*, 56-1–56-4. [[CrossRef](#)]
59. Goodwin, A.M. Chapter 3—Early Proterozoic Crust. In *Principles of Precambrian Geology*; Goodwin, A.M., Ed.; Academic Press: London, UK, 1996; pp. 123–176. [[CrossRef](#)]
60. Lucas, S.B.; St-Onge, M.R. *Geology of the Precambrian Superior and Grenville Provinces and Precambrian Fossils in North America*; Geological Society of America: Boulder, CO, USA, 1998.
61. Purucker, M.E.; Langel, R.A.; Rajaram, M.; Raymond, C. Global magnetization models with a priori information. *J. Geophys. Res. Solid Earth* **1998**, *103*, 2563–2584. [[CrossRef](#)]
62. Masterton, S.M.; Gubbins, D.; Mueller, R.D.; Singh, K.H. Forward modelling of oceanic lithospheric magnetization. *Geophys. J. Int.* **2012**, *192*, 951–962. [[CrossRef](#)]
63. Finlay, C.; Olsen, N.; Kotsiaros, S.; Gillet, N.; Tøffner-Clausen, L. Recent geomagnetic secular variation from Swarm and ground observatories as estimated in the CHAOS-6 geomagnetic field model. *Earth Planets Space* **2016**, *68*, 112. [[CrossRef](#)]
64. Artemieva, I.; Mooney, W. Thermal thickness and evolution of Precambrian lithosphere: A global study. *J. Geophys.-Res.-Solid Earth* **2001**, *106*, 16387–16414. [[CrossRef](#)]
65. Fox Maule, C. Geophysical Interpretation of Magnetic Field Models. Ph.D. Thesis, University of Copenhagen, Faculty of Science, København, Denmark, 2005.
66. Jaupart, C.; Mareschal, J.C. The thermal structure and thickness of continental roots. *Dev. Geotecton.* **1999**, *24*, 93–114. [[CrossRef](#)]
67. Jaupart, C.; Mareschal, J.C.; Iarotsky, L. Radiogenic heat production in the continental crust. *Lithos* **2016**, *262*, 398–427. [[CrossRef](#)]
68. Drury, M.J. The heat flow—heat generation relationship: Implications for the nature of continental crust. *Tectonophysics* **1989**, *164*, 93–106. [[CrossRef](#)]
69. Pribnow, D.; Winter, H. Radiogenic heat production in the upper third of continental crust from KTB. *Geophys. Res. Lett.* **1997**, *24*, 349–352. [[CrossRef](#)]
70. Howell, S.M.; Ito, G.; Breivik, A.J.; Rai, A.; Mjelde, R.; Hanan, B.; Sayit, K.; Vogt, P. The origin of the asymmetry in the Iceland hotspot along the Mid-Atlantic Ridge from continental breakup to present-day. *Earth Planet. Sci. Lett.* **2014**, *392*, 143–153. [[CrossRef](#)]
71. Dordevic, M.; Georgen, J. Dynamics of plume-triple junction interaction: Results from a series of three-dimensional numerical models and implications for the formation of oceanic plateaus. *J. Geophys. Res. Solid Earth* **2016**, *121*, 1316–1342. [[CrossRef](#)]

72. Heyn, B.H.; Conrad, C.P. On the Relation Between Basal Erosion of the Lithosphere and Surface Heat Flux for Continental Plume Tracks. *Geophys. Res. Lett.* **2022**, *49*, e2022GL098003. [[CrossRef](#)]
73. Rogozhina, I.; Petrunin, A.G.; Vaughan, A.P.; Steinberger, B.; Johnson, J.V.; Kaban, M.K.; Calov, R.; Rickers, F.; Thomas, M.; Koulakov, I. Melting at the base of the Greenland ice sheet explained by Iceland hotspot history. *Nat. Geosci.* **2016**, *9*, 366–369. [[CrossRef](#)]
74. Fahnestock, M.; Abdalati, W.; Joughin, I.; Brozena, J.; Gogineni, P. High geothermal heat flow, basal melt, and the origin of rapid ice flow in central Greenland. *Science* **2001**, *294*, 2338–2342. [[CrossRef](#)] [[PubMed](#)]
75. Toyokuni, G.; Matsuno, T.; Zhao, D. P Wave Tomography Beneath Greenland and Surrounding Regions: 2. Lower Mantle. *J. Geophys. Res. Solid Earth* **2020**, *125*, e2020JB019839. [[CrossRef](#)]

**Disclaimer/Publisher’s Note:** The statements, opinions and data contained in all publications are solely those of the individual author(s) and contributor(s) and not of MDPI and/or the editor(s). MDPI and/or the editor(s) disclaim responsibility for any injury to people or property resulting from any ideas, methods, instructions or products referred to in the content.